CrossMark

J. Fluid Mech. (2016), *vol.* 803, *pp.* 466–501. © Cambridge University Press 2016
doi:10.1017/jfm.2016.509

Optimal perturbations in time-dependent variable-density Kelvin–Helmholtz billows

Adriana Lopez-Zazueta[1], Jérôme Fontane[1,†] and Laurent Joly[1]

[1]Institut Supérieur de l'Aéronautique et de l'Espace (ISAE-SUPAERO), Université de Toulouse, 10 avenue Édouard Belin - BP 54032 - 31055 Toulouse CEDEX 4, France

(Received 22 January 2016; revised 10 June 2016; accepted 26 July 2016; first published online 30 August 2016)

We analyse the influence of the specific features of time-dependent variable-density Kelvin–Helmholtz (VDKH) roll-ups on the development of three-dimensional secondary instabilities. Due to inertial (high Froude number) baroclinic sources of spanwise vorticity at high Atwood number (up to 0.5 here), temporally evolving mixing layers exhibit a layered structure associated with a strain field radically different from their homogeneous counterpart. We use a direct-adjoint non-modal linear approach to determine the fastest growing perturbations over a single period of the time-evolving two-dimensional base flow during a given time interval $[t_0, T]$. When perturbations are seeded at the initial time of the primary KH mode growth, i.e. $t_0 = 0$, it is found that additional mechanisms of energy growth are onset around a bifurcation time t_b, a little before the saturation of the primary two-dimensional instability. The evolution of optimal perturbations is thus observed to develop in two distinct stages. Whatever the Atwood number, the first period $[t_0, t_b]$ is characterised by a unique route for optimal energy growth resulting from a combination of the Orr and lift-up transient mechanisms. In the second period $[t_b, T]$, the growing influence of mass inhomogeneities raises the energy gain over the whole range of spanwise wavenumbers. As the Atwood number increases, the short spanwise wavelength perturbations tend to benefit more from the onset of variable-density effects than large wavelength ones. The extra energy gain due to increasing Atwood numbers relies on contributions from spanwise baroclinic sources. The resulting vorticity field is structured into two elongated dipoles localised along the braid on either side of the saddle point. In return they yield two longitudinal velocity streaks of opposite sign which account for most of the energy growth. This transition towards three-dimensional motions is in marked contrast with the classic streamwise rib vortices, so far accepted as the paradigm for the transition of free shear flows, either homogeneous or not. It is argued that the emergence of these longitudinal velocity streaks is generic of the transition in variable-density shear flows. Among them, the light round jet is known to display striking side ejections as a result of the loss of axisymmetry. The present analysis helps to renew the question of the underlying flow structure behind side jets, otherwise based on radial induction between pairs of counter-rotating longitudinal vortices (Monkewitz & Pfizenmaier, *Phys. Fluids* A, vol. 3 (5), 1991, pp. 1356–1361). Instead, it is more likely that side ejections would result from the convergence of the longitudinal velocity streaks near the braid saddle point. When the injection time is delayed so as to suppress the initial stage of energy growth, a new class of perturbations arises at low wavenumber with energy

† Email address for correspondence: j.fontane@isae.fr

https://doi.org/10.1017/jfm.2016.509 Published online by Cambridge University Press

gains far larger than those observed so far. They correspond to the two-dimensional Kelvin–Helmholtz secondary instability of the baroclinically enhanced vorticity braid discovered by Reinaud *et al.* (*Phys. Fluids*, vol. 12 (10), pp. 2489–2505), leading potentially to another route to turbulence through a two-dimensional fractal cascade.

Key words: free shear layers, instability, jets

1. Introduction

Flows of interest to industrial applications or occurring spontaneously in nature are seldom homogeneous. Gas flows over obstacles at high velocities are subjected to temperature variations and density conditions due to the gas compressibility, but low-speed flows involved in heat transfer or in species mixing are subjected to non-homogeneous inlet or boundary conditions resulting also in density variations in the bulk flow itself. The density contrast, namely the Atwood number $At \sim \Delta\rho/\rho_0$ which measures characteristic density variations $\Delta\rho$ around a mean value ρ_0, may be very small but in geophysical flows, immersed in a gravity field, buoyancy still drives the flow and their governing equations are liable to the Boussinesq approximation. For pairs of highly density-contrasted fluids, such as fuel–oxidiser candidates (i.e. methane–air or hydrogen–oxygen), the Atwood number increases well beyond the Boussinesq approximation. In these flows, the buoyancy plays no significant role and the vortex dynamics is affected by inertial baroclinic vorticity production and also departs largely from its homogeneous counterpart (Soteriou & Ghoniem 1995; Fontane & Joly 2008; Dixit & Govindarajan 2010).

As locally relevant to more complex flows, the mixing-layer prototype, and its temporally evolving subset, is of central interest to these variable-density mixing flows. The linear stability analysis of a sheared density interface, hinted at by Batchelor (1967), was performed early by Davey & Roshkom (1972), but the stability of a sheared (smooth) density-gradient layer awaited the contribution of Soteriou & Ghoniem (1995) even recovering the shift of the phase velocity towards the heaviest fluid that was already observed in the discontinuous case. Most important to the present work, the latter paper came with a clear schematic view of distributed baroclinic sources and sinks of spanwise vorticity altering the structure of the homogeneous Kelvin–Helmholtz (KH) roll-up. As stressed later by Joly (2002), baroclinic vorticity production in the KH roll-up promotes a layered vorticity structure eventually replacing the billow with thin and wrapped vorticity sheets of alternate signs as the Atwood number is increased. The question emerged of the effect of this spanwise vorticity redistribution in the variable-density Kelvin–Helmholtz billow (hereinafter quoted VDKH) on its transition to three-dimensional motions.

Side ejections observed in light round jets (Monkewitz *et al.* 1989, 1990) are one clear manifestation of the specific feature of the variable-density free shear flow transition. The mechanism for the generation of these side jets received a first proposition from Monkewitz & Pfizenmaier (1991) which was corroborated by Brancher, Chomaz & Huerre (1994) in the homogeneous situation without resorting to baroclinically modified vortex rings or to baroclinic vorticity contributions to non-azimuthal vorticity. In the plane shear-layer case, three-dimensional simulations (Knio & Ghoniem 1992; Joly, Reinaud & Chassaing 2001) gave no clear answers to the above question and only acknowledged increased growth rates of arbitrarily

https://doi.org/10.1017/jfm.2016.509 Published online by Cambridge University Press

simple (non-optimal) counter-rotating streamwise vortices simply derived from the consensus on secondary instabilities as was done in the homogeneous mixing layer (Rogers & Moser 1992). A first attempt was made by Joly, Suarez & Chassaing (2003) to quantify the modifications of the strain field in light jets and their impact on the transient growth of three-dimensional modes following the framework proposed by Caulfield & Kerswell (2000). It was concluded that the growth rates of transient modes in light jet vortex rings were double those of their homogeneous counterparts, before and during the pairing process. It was not until the work of Fontane & Joly (2008) that the global modal stability of the VDKH billow, of the same kind as the one derived before by Klaassen & Peltier (1991) for both the homogeneous and stratified mixing layers, was addressed straightforwardly. The linear response of the plane VDKH billow was demonstrated to be rich of a whole set of new secondary modes together with classical elliptical and hyperbolic modes, the latter exhibiting higher growth rates than those developing within the homogeneous KH roll-up. Furthermore, the two-dimensional secondary KH instability of the baroclinically enhanced vorticity braid, elucidated by Reinaud, Joly & Chassaing (2000), was recovered in this linear analysis. However, the quasi-static approach based on a frozen approximation of the unsteady two-dimensional base flow is valid only for perturbations growing faster than the time scale of the base-flow unsteadiness, which is a strong limitation. Given that these time scales are not clearly separated and that transient growth may benefit from the non-normality of the evolution operator, there is a need to carry out a linear direct-adjoint non-modal analysis, well suited to determine the optimal energy growth of small perturbations over a temporally evolving VDKH billow. This is the aim of the present work which can be considered to be a generalisation of the work Arratia, Caulfield & Chomaz (2013) on homogeneous mixing layers to a variable-density situation.

In the homogeneous case, it is now well established that the KH roll-up is susceptible to two types of secondary instabilities (Klaassen & Peltier 1991; Caulfield & Peltier 2000; Fontane & Joly 2008): a small wavenumber core-centred elliptical instability, originally coined by Pierrehumbert & Widnall (1982) as the 'translative instability' due to the induced spanwise displacement of the vortex core, and a large wavenumber braid-centred hyperbolic instability. From experimental and numerical evidence, the three-dimensionalisation of the flow is associated with the emergence of streamwise rib vortices in the braid region (see Corcos & Lin 1984, Metcalfe *et al.* 1987, Lasheras & Choi 1988, Rogers & Moser 1992 amongst others). Therefore, this strongly suggests that the hyperbolic instability is at the origin of the flow transition to three-dimensional motions. However, the picture is not that simple since a spanwise undulation of the KH vortex core is also observed during the transition and thus could result from the development of an elliptic instability. The commonly accepted view is that the spanwise undulation of the KH vortex core is the direct consequence of the wrapping of the longitudinal rib vortices around the primary vortex billow. Nevertheless, it does not give an answer to whether the elliptic or the hyperbolic modes are responsible for the three-dimensionalisation of the flow. This point stayed an opened question for a long time and Rogers & Moser (1992) even concluded that the correct point of view would be to consider the combination of both instabilities as a global mode that would lead to the simultaneous growth of three-dimensional perturbations in the vortex core and in the braid. The recent non-modal stability analysis of Arratia *et al.* (2013) seems to confirm that proposal. Indeed, they observed two classes of three-dimensional optimal perturbations for time horizons beyond the saturation of the primary KH wave. A so-called E-type

https://doi.org/10.1017/jfm.2016.509 Published online by Cambridge University Press

perturbation at low wavenumber giving rise to the elliptic core-centred instability and a so-called H-type mode at large wavenumber leading to the development of the braid-centred hyperbolic instability. Both types of perturbations grow initially thanks to a combination of the Orr (1907*a*,*b*) and lift-up (Ellingsen & Palm 1975; Landhal 1975, 1980) mechanisms of transient energy growth and exhibit streamwise rib vortices before eventually triggering the elliptic or the hyperbolic instabilities. The E-type is the global optimal when perturbations are injected from the initial development of the flow while the H-type becomes dominant only when the optimisation interval starts after the initial period of transient growth. The selection of an E-type rather than an H-type of perturbation depends on the spanwise wavenumber of the initial perturbation but in both cases, the response to these perturbations takes the form of rib vortices in the braid region.

In stratified mixing layers, the transition to three-dimensional motions is also related to the development of streamwise rib vortices but they originate from a different physical mechanism associated with a different family of secondary instabilities (Klaassen & Peltier 1985, 1991; Caulfield & Peltier 2000). These secondary modes, coined convective instabilities, are located within the periphery of the primary KH vortex core in 'superadiabatic' regions where the initial stable stratification has been locally reversed due to the roll-up of the shear layer. They derive their energy growth essentially from potential energy conversion and their spanwise wavenumber and growth rates increase with the initial Richardson number, compared to the ones of the homogeneous hyperbolic instabilities (Caulfield & Peltier 2000). Their nonlinear evolution leads to longitudinal vortex streaks which eventually extend along the braid of the KH primary structure as observed both experimentally (Schowalter, Van Atta & Lasheras 1994) and numerically (Cortesi, Yadigaroglu & Banerjee 1998; Caulfield & Peltier 2000). These modes were uncovered through a global modal stability analysis using a quasi-static approach and assuming that the unsteadiness of the two-dimensional stratified KH billows could be neglected. As for the high Froude number variable-density KH billows, this approximation needs to be examined further by means of a linear direct-adjoint non-modal analysis. The recent work of Kaminski, Caulfield & Taylor (2014) focuses only on transient growths occurring over the parallel stratified shear layer. In agreement with the results of Arratia *et al.* (2013) obtained in the homogeneous case, they found that short-time optimal perturbations are fully three-dimensional oblique waves relying on the lift-up and Orr mechanisms (Farrell & Ioannou 1993) while the two-dimensional KH instability is the optimal perturbation for the long-time horizon when the Richardson number is small enough. Conversely, when the initial Richardson number is higher and prevents the growth of any modal instability, transient growth associated with the excitation of internal waves outside the vorticity layer was observed. Apart from this recent study, there is no equivalent non-modal analysis for secondary instabilities developing in stratified mixing layers equivalent to the one conducted by Arratia *et al.* (2013) in the homogeneous case, and to which we could compare our results obtained in the present work.

In the case of the variable-density mixing layer, are streamwise rib vortices still the relevant ingredient of the transition to three-dimensional motions? Which of the mechanisms behind the three types of modes (elliptic, hyperbolic and secondary KH), observed in the modal analysis of Fontane & Joly (2008), are most efficient for perturbation growth over an unsteady VDKH billow? The present work aims to answer these questions through a non-modal stability analysis similar to that of Arratia *et al.* (2013).

https://doi.org/10.1017/jfm.2016.509 Published online by Cambridge University Press

The paper is organised as follows. The governing equations and the numerical simulation leading to the generation of the nonlinear VDKH wave are briefly presented in § 2. We also describe the particular features of the base flow that are relevant to the development of three-dimensional motions. The section ends with the derivation of the equations for the linear direct-adjoint three-dimensional linear non-modal stability analysis. The numerical method to solve this problem is detailed and validated in the same section. The results of the non-modal stability analysis of the variable-density mixing layer are detailed in the next section and compared to the results of Arratia *et al.* (2013) in the homogeneous case. They focus on the influence on the optimal perturbation of the Atwood number and of the optimisation interval (both the injection and horizon times). The paper ends with conclusions and perspectives.

2. Formulation of the problem

2.1. *Governing equations*

We consider an incompressible binary mixing of two species of density ρ_1 and ρ_2 respectively, with $\rho_2 > \rho_1$. We denote respectively ℓ_0, u_0 and $\rho_0 = (\rho_1 + \rho_2)/2$ the characteristic length, velocity and density scales. In the limit of zero Mach number, the equation of state can be combined with both the continuity equation and the transport equation of the mass fraction of one of the species to show that the non-solenoidal part of the velocity field is of a diffusive nature (Joseph 1990; Sandoval 1995),

$$\boldsymbol{\nabla}\cdot\boldsymbol{u} = -\frac{1}{Re\,Sc}\boldsymbol{\nabla}\cdot\left(\frac{1}{\rho}\boldsymbol{\nabla}\rho\right), \tag{2.1}$$

where $Re = (u_0\ell_0\rho_0)/\mu$ and $Sc = \mu/\rho_0\mathscr{D}$ are the Reynolds and Schmidt numbers with μ the dynamic viscosity of the mixing and $\mathscr{D}$ the Fickian diffusivity of one of the species into the other. We consider μ and $\mathscr{D}$ to be constant, which is a fair approximation for a binary mixing of perfect gases, see Fontane (2005) for the specific case of the air–helium couple. The relevant parameter of the inertia effect is the Froude number $Fr = u_0/\sqrt{g\ell_0 At}$ in which the Atwood number is defined by $At = \Delta\rho/\rho_0$ where $\Delta\rho = (\rho_2 - \rho_1)/2$ is the scale for the density difference. As we address buoyancy-free flows, the Froude number is assumed to be large, i.e. $Fr \gg 1$, and the dimensionless Navier–Stokes equations read

$$D_t\rho = \frac{\rho}{Re\,Sc}\boldsymbol{\nabla}\cdot\left(\frac{1}{\rho}\boldsymbol{\nabla}\rho\right), \tag{2.2}$$

$$\rho D_t\boldsymbol{u} = -\boldsymbol{\nabla}p + \frac{1}{Re}\boldsymbol{\Delta}\boldsymbol{u} + \frac{1}{3Re}\boldsymbol{\nabla}\,(\boldsymbol{\nabla}\cdot\boldsymbol{u}), \tag{2.3}$$

where $D_t = \partial_t + (\boldsymbol{u}\cdot\boldsymbol{\nabla})$ stands for the material derivative. The corresponding vorticity equation is obtained by taking the curl of the momentum equation (2.3)

$$D_t\boldsymbol{\omega} = \boldsymbol{\omega}\cdot\boldsymbol{\nabla}\boldsymbol{u} - \boldsymbol{\omega}\boldsymbol{\nabla}\cdot\boldsymbol{u} + \frac{1}{\rho^2}\boldsymbol{\nabla}\rho\times\boldsymbol{\nabla}p + \frac{1}{Re}\boldsymbol{\Delta}\boldsymbol{\omega}, \tag{2.4}$$

where the third term on the right-hand side is the baroclinic torque $\boldsymbol{b} = (1/\rho)\boldsymbol{\nabla}\rho\times(1/\rho)\boldsymbol{\nabla}p$ which becomes active for misaligned isopycnals and isobars. It is responsible for the specific features of the variable-density flows considered here and will be of central interest in the following. In the inviscid limit, it can be rewritten as the

https://doi.org/10.1017/jfm.2016.509 Published online by Cambridge University Press

cross-product between the acceleration of the flow itself $\boldsymbol{a} = D_t\boldsymbol{u} = -(1/\rho)\boldsymbol{\nabla} p$ and the density gradient

$$\boldsymbol{b} = \boldsymbol{a} \times \frac{1}{\rho}\boldsymbol{\nabla}\rho, \tag{2.5}$$

which stresses the particular nature of the baroclinic vorticity production considered here compared to stratified geophysical flows where the flow acceleration is replaced by the gravity acceleration $\boldsymbol{g}$.

2.2. *The time-dependent VDKH roll-ups*

The two-dimensional base flow consists of a time-evolving shear layer between two fluids of different density which undergoes the development of a KH instability biased by the density contrast. It is obtained through direct numerical simulations using a two-dimensional dealiased pseudo-spectral method described in detail in Joly, Fontane & Chassaing (2005) and Joly & Reinaud (2007). The x and y axes correspond to the longitudinal and crosswise directions. The spanwise direction along the z-axis will only serve for the subsequent non-modal stability analysis. Since co-gradient and counter-gradient variable-density mixing layers are equivalent in the frame of temporal approximation at infinite Froude number (Fontane & Joly 2008), we arbitrarily choose a co-gradient mixing layer by placing the lighter fluid in the lower part of the flow. We take u_0 as half the velocity difference across the shear layer and ℓ_0 as half the vorticity thickness of the shear layer as characteristics velocity and length scales. The normalised profiles of velocity $\overline{\boldsymbol{U}} = (\overline{U}_x, 0)$ and density $\overline{R}$ of the initial variable-density parallel shear flow are:

$$\overline{U}_x(y) = \tanh(y), \tag{2.6a}$$

$$\overline{R}(y) = 1 + At\ \tanh(y). \tag{2.6b}$$

This flow is perturbed by the most unstable mode of the inviscid temporal linear stability analysis as described in Fontane & Joly (2008). Its amplitude is prescribed such that the enstrophy of the perturbation is a small fraction of the enstrophy of the parallel shear layer over a period. The value a_{KH} of this fraction is set so that the primary KH instability saturates at $t_{KH} = 30$. The two-dimensional velocity $\boldsymbol{U} = (U_x, U_y)$ and density R fields are calculated on the domain $[0, L_x] \times [-L_x/2, L_x/2]$. The initial thickness of the shear layer is set so that the most amplified KH mode corresponds to a wavenumber of $2\pi/L_x$. The boundary conditions are periodic in the longitudinal direction while a free-slip boundary condition is imposed in the crosswise direction. The vertical extent of the domain is large enough so that the free-slip wall do not strongly affect the nonlinear development of the flow (Fontane & Joly 2008). We focus specifically on the influence of density effects on the development of secondary instabilities and we vary the Atwood number while both Reynolds and Schmidt numbers are fixed to $Re = 1000$ and $Sc = 1$. The same value of the Reynolds number has been used in the work of Arratia *et al.* (2013) to which we compare our results. It is also representative of the values for which side jets naturally arise in light jets (Monkewitz & Pfizenmaier 1991; Fontane 2005). For all simulations, we use a mesh of 512^2 points, which has been checked to be large enough to ensure convergence of the results. Note that the number of points used here is far smaller than the ones used by Fontane & Joly (2008) in the infinite Schmidt number case where the absence of mass diffusion induces the need for a constantly growing spatial resolution. All these numerical settings are summarised in table 1.

https://doi.org/10.1017/jfm.2016.509 Published online by Cambridge University Press

At	$S=\rho_2/\rho_1$	Re	Sc	ℓ_0	a_{KH}	L_x/ℓ_0	$N_x \times N_y$
0	1	1000	—	0.4449	0.0222	14.12	512^2
0.05	1.1	1000	1	0.4454	0.0222	14.11	512^2
0.25	1.67	1000	1	0.4582	0.0215	13.71	512^2
0.5	3	1000	1	0.4978	0.0190	12.62	512^2

TABLE 1. Main numerical parameters for the four simulated VDKH base-flow fields: Atwood number At, density ratio $S=\rho_2/\rho_1$, Reynolds number Re, Schmidt number Sc, half the initial vorticity thickness ℓ_0, fraction a_{KH} of the initial enstrophy of the KH mode relative to the enstrophy of the parallel shear layer, ratio L_x/ℓ_0 between the domain size and half the initial vorticity thickness, mesh size $N_x \times N_y$.

As will be confirmed later in § 3, the inner roll-up structure has a strong influence on the characteristics of the secondary perturbations. Hence, we now briefly describe the specific feature of the VDKH billow compared to the classic homogeneous KH roll-up. Figures 1(*a*) and 1(*c*) display the vorticity field at saturation time $t_{KH}=30$ for the homogeneous case $At=0$ and the most density-contrasted case $At=0.5$. In the later, not only the vorticity field has lost its symmetry but it also concentrates into two sheets of opposite sign on either side of the braid saddle point. This reorganisation of the vorticity field is the consequence of the baroclinic multi-polar source–sink system advocated by Soteriou & Ghoniem (1995) and Reinaud *et al.* (2000) and illustrated in figure 1(*f*). In this figure, we represent the acceleration and density gradient near the two main source and sink patches in order to illustrate the local contribution of the baroclinic torque according to its inviscid approximation (2.5). The baroclinic vorticity production induces also a slight asymmetry in the density field which results in a preferential entrainment of the light fluid towards the heavy flow as seen in figure 1(*e*). Another consequence of the baroclinic vorticity redistribution lies in a drastic change in the strain field. Following Caulfield & Kerswell (2000), the strain field ϵ of the base flow defined as

$$\epsilon(x,y)=\sqrt{\frac{1}{4}\left(\frac{\partial U_x}{\partial y}+\frac{\partial U_y}{\partial x}\right)^2-\frac{\partial U_x}{\partial x}\frac{\partial U_y}{\partial y}} \tag{2.7}$$

is plotted at t_{KH} in figures 1(*b*) and 1(*d*) for the homogeneous case and the most density-contrasted case respectively. The evolution of its structure follows the reorganisation of the vorticity field: it is progressively concentrated and intensified within the two vorticity-enhanced layers on either side of the braid hyperbolic point as the Atwood number is increased. The levels of strain reached there are significantly higher than in the homogeneous case. This is confirmed in figure 2 where the evolution of the maximum strain rate is plotted for the four Atwood numbers considered. While the maximum strain rate is decreasing in the homogeneous case after $t=20$, it is increasing for large Atwood number. At saturation of the primary KH instability, the measured value is three times higher for $At=0.5$ than in the homogeneous case.

Compared to its homogeneous counterpart, the VDKH billow exhibits an asymmetric layered vorticity field holding much higher levels of strain. Vorticity being generated on thin layers associated with length scales smaller than the ones found in the smooth homogeneous base flow, an increase in Atwood number is likely to promote energy growth for larger spanwise wavenumbers.

https://doi.org/10.1017/jfm.2016.509 Published online by Cambridge University Press

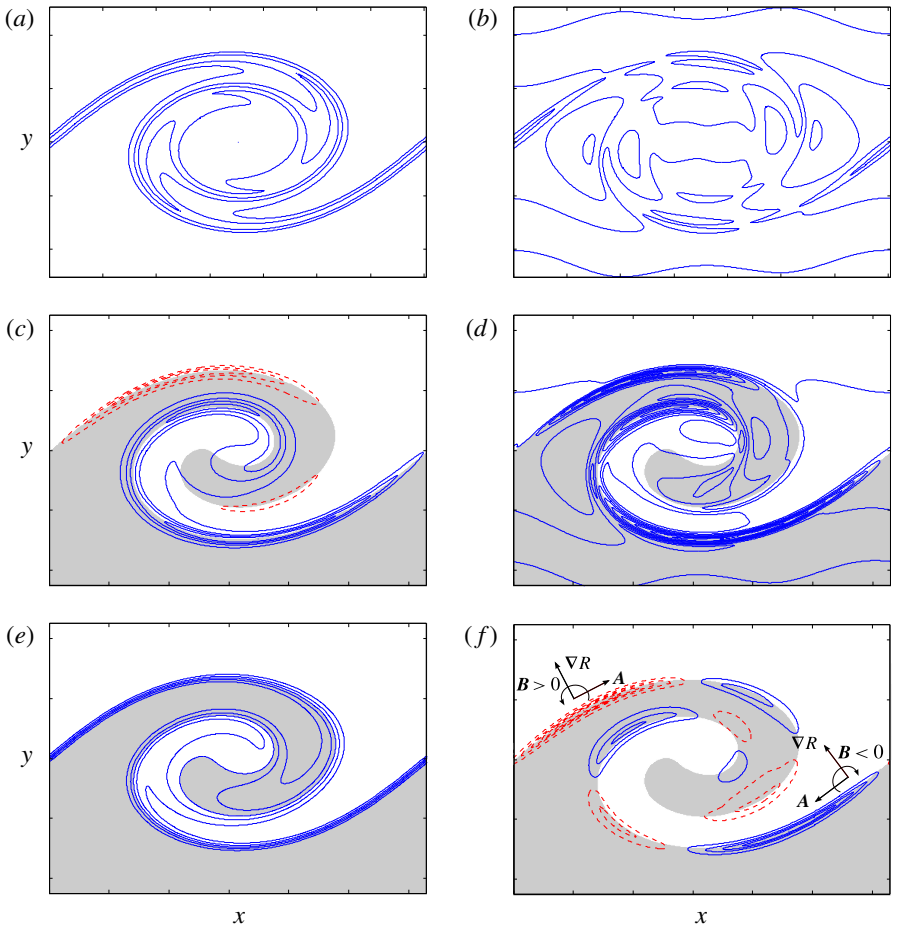


FIGURE 1. (Colour online) Base-flow characteristics at the saturation time $t_{KH} = 30$: (*a*) spanwise vorticity field for $At = 0$, (*b*) strain field for $At = 0$, (*c*) spanwise vorticity field for $At = 0.5$, (*d*) strain field for $At = 0.5$, (*e*) density field for $At = 0.5$ and (f) spanwise baroclinic torque for $At = 0.5$. In figures (*c*)–(*f*), the grey-shaded region corresponds to the domain where the base-flow density is lower than ρ_0 and dashed contours correspond to positive values. In all figures, tick marks along x and y axis are separated by the initial vorticity thickness $\delta^0_\omega = 2l_0$. These conventions will hold throughout the paper.

2.3. *Optimisation problem*

We now consider the linear evolution of three-dimensional perturbations $[\boldsymbol{u}, \rho, p]$ that are likely to develop on top of the VDKH billows $[\boldsymbol{U}, R, P]$. We linearise the governing equations (2.1)–(2.3) around the two-dimensional base flow:

$$\frac{\partial \boldsymbol{u}}{\partial t} + \boldsymbol{U}\cdot\boldsymbol{\nabla}\boldsymbol{u} + \boldsymbol{u}\cdot\boldsymbol{\nabla}\boldsymbol{U} = -\frac{1}{R}\boldsymbol{\nabla}p + \frac{\rho}{R^2}\boldsymbol{\nabla}P + \frac{1}{Re\,R}\left(\boldsymbol{\Delta}\boldsymbol{u} + \frac{1}{3}\boldsymbol{\nabla}d\right) - \frac{\rho}{Re\,R^2}\left(\boldsymbol{\Delta}\boldsymbol{U} + \frac{1}{3}\boldsymbol{\nabla}D\right), \tag{2.8a}$$

$$\frac{\partial \rho}{\partial t} + \boldsymbol{U}\cdot\boldsymbol{\nabla}\rho + \boldsymbol{u}\cdot\boldsymbol{\nabla}R + \rho D = -Rd, \tag{2.8b}$$

https://doi.org/10.1017/jfm.2016.509 Published online by Cambridge University Press

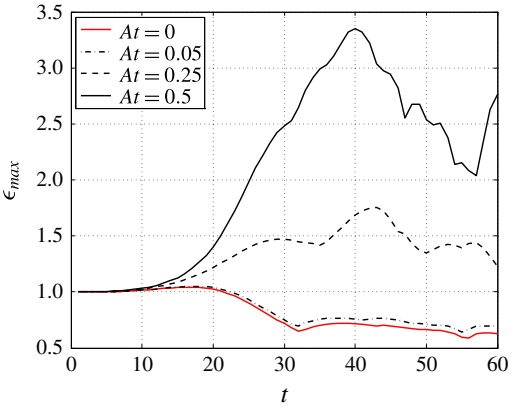


FIGURE 2. (Colour online) Influence of the Atwood number on the temporal evolution of the maximum value ϵ_{max} of the base-flow strain rate normalised by its initial value.

$$d = -\frac{1}{Re\,Sc}\boldsymbol{\Delta}\left(\frac{\rho}{R}\right), \tag{2.8c}$$

where $D = \boldsymbol{\nabla}\cdot\boldsymbol{U}$ and $d = \boldsymbol{\nabla}\cdot\boldsymbol{u}$. This linear system – referred to as the direct system – can be cast in the following compact form:

$$\boldsymbol{N}_t\cdot\boldsymbol{q} + \boldsymbol{N}_c\cdot\boldsymbol{q} + \frac{1}{Re}\boldsymbol{N}_d\cdot\boldsymbol{q} = 0, \tag{2.9}$$

where $\boldsymbol{q} = [\boldsymbol{u},\ \rho,\ p]$ and the three matrix operators are respectively the temporal operator $\boldsymbol{N}_t$, the operator of coupling between the base flow and the perturbation $\boldsymbol{N}_c$ and the diffusion operator $\boldsymbol{N}_d$. Their expressions are detailed in appendix A.

In the frame of non-modal stability analysis, the temporal behaviour is not prescribed, and taking into account the streamwise periodicity and the spanwise homogeneity of the base flow, the perturbations are sought under the form

$$[u_x,\ u_y,\ u_z,\ \rho,\ p](x,\ y,\ z,\ t) = \tfrac{1}{2}[\tilde{u}_x,\ \tilde{u}_y,\ i\tilde{u}_z,\ \tilde{\rho},\ \tilde{p}](x,\ y,\ t)\mathrm{e}^{\mathrm{i}(\mu x+kz)} + \text{c.c.}, \tag{2.10}$$

where k is the real spanwise wavenumber and $\mu \in [0,\ 1]$ the real Floquet exponent. Note that the spanwise velocity component is phase shifted with respect to the two other velocity components in order to satisfy the mass continuity equation. We restrict here the search for perturbations that have the same longitudinal periodicity as the base flow, i.e. $\mu = 0$. This is motivated by the experimental evidence that three-dimensional structures appearing in mixing layers and round jets develop in between two consecutive KH billows. Furthermore, Klaassen & Peltier (1991) and Fontane & Joly (2008) reported that the most unstable modes of both stratified and inhomogeneous mixing layers did not vary appreciably with non-zero Floquet exponent.

Amongst all possible perturbations likely to grow over the VDKH billow, we focus on those maximising the kinetic energy gain over a given period of time $[t_0,\ T]$:

$$G_E(T,\ t_0) = \frac{E(T)}{E(t_0)} = \frac{\|\boldsymbol{q}(T)\|_u}{\|\boldsymbol{q}(t_0)\|_u}, \tag{2.11}$$

https://doi.org/10.1017/jfm.2016.509 Published online by Cambridge University Press

where t_0, T are respectively called injection and horizon times and $\|\cdot\|_u$ denotes the semi-norm associated with the conventional inner product yielding the kinetic energy, see appendix B. Following the seminal work of Farrell (1988), we look for the 'optimal perturbation' which reaches the maximal energy gain

$$\mathscr{G}_E(T, t_0) = \max_{\boldsymbol{q}(t_0)}\{G_E(T, t_0)\} \tag{2.12}$$

over all the possible initial conditions $\boldsymbol{q}(t_0)$. Its determination resorts to solving an optimisation problem with constraints (Gunzburger 2003) enforcing the perturbation to be a solution of the linearised NS equations (2.8). The problem can be classically transformed into an optimisation problem without constraint using the variational method of the Lagrange multipliers, see for example Luchini & Bottaro (1998) or Corbett & Bottaro (2000, 2001). This requires the derivation of the so-called adjoint equations (Schmid 2007). In the specific context of incompressible inhomogeneous flow at large Froude number, we believe that this is the first time that such an adjoint system is needed. It has been derived here for the equations (2.8),

$$-\frac{\partial \boldsymbol{u}^\dagger}{\partial t} - \boldsymbol{U}\cdot\boldsymbol{\nabla}\boldsymbol{u}^\dagger - \boldsymbol{u}^\dagger\boldsymbol{\nabla}\cdot\boldsymbol{U} + \boldsymbol{\nabla}\boldsymbol{U}^{\mathrm{T}}\cdot\boldsymbol{u}^\dagger = \boldsymbol{\nabla}p^\dagger + R\boldsymbol{\nabla}\rho^\dagger + \frac{1}{Re}\boldsymbol{\Delta}\left(\frac{\boldsymbol{u}^\dagger}{R}\right) + \frac{1}{3Re}\boldsymbol{\nabla}d^\dagger, \tag{2.13a}$$

$$-\frac{\partial \rho^\dagger}{\partial t} - \boldsymbol{U}\cdot\boldsymbol{\nabla}\rho^\dagger = \frac{1}{R^2}\boldsymbol{u}^\dagger\cdot\left(\boldsymbol{\nabla}P - \frac{1}{Re}\boldsymbol{\Delta}\boldsymbol{U} - \frac{1}{3Re}\boldsymbol{\nabla}D\right) + \frac{1}{Re\,Sc\,R}\boldsymbol{\Delta}p^\dagger, \tag{2.13b}$$

$$d^\dagger = \boldsymbol{\nabla}\cdot\left(\frac{\boldsymbol{u}^\dagger}{R}\right) = 0, \tag{2.13c}$$

where $\boldsymbol{u}^\dagger$, $p^\dagger$ and $\rho^\dagger$ are the corresponding adjoint variables of the velocity, the pressure and the density fields respectively and $^{\mathrm{T}}$ stands for matrix transpose. As for the direct system (2.8), the adjoint system can be reduced to the following compact form:

$$-\boldsymbol{N}_t\cdot\boldsymbol{q}^\dagger + \boldsymbol{N}_c^\dagger\cdot\boldsymbol{q}^\dagger + \frac{1}{Re}\boldsymbol{N}_d^\dagger\cdot\boldsymbol{q}^\dagger = 0, \tag{2.14}$$

where $\boldsymbol{q}^\dagger = [\boldsymbol{u}^\dagger, \rho^\dagger, p^\dagger]$. As is commonly understood, the evolution of this dynamical system requires a backward-in-time integration as signified by the minus sign before the temporal operator $\boldsymbol{N}_t$. The expressions for the two matrix operators $\boldsymbol{N}_c^\dagger$ and $\boldsymbol{N}_d^\dagger$ are given in appendix A.

The determination of the optimal perturbation and the associated optimal energy gain $\mathscr{G}_E$ relies on an iterative optimisation algorithm. An initial condition $\boldsymbol{q}(t_0)$ chosen as a white noise is integrated forward in time until the horizon time T using the direct system (2.9). The initial white noise condition can be applied to every field of the perturbation, but we restrict it here to the velocity field since the objective is to maximise the kinetic energy gain from a purely kinematic initial perturbation. We did try a non-zero initial density perturbation but the results did not vary significantly with respect to the energy gain and the structure of optimal perturbations against the case with no initial density perturbation. The resulting final state is used to compute the initial condition $\boldsymbol{q}^\dagger(T)$ for the adjoint system (2.14) which is integrated backward-in-time up to the injection time t_0. After appropriate rescaling in order to satisfy the chosen normalisation of the perturbation (see appendix B), this final state is used for the next direct-adjoint integration. Multiple iterations of this loop lead

https://doi.org/10.1017/jfm.2016.509 Published online by Cambridge University Press

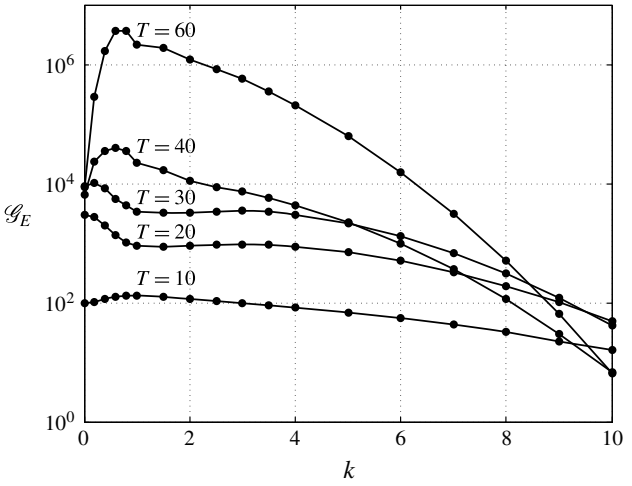


FIGURE 3. Influence of the horizon time T on the optimal energy gain $\mathscr{G}_E$ as a function of the spanwise wavenumber k of the optimal perturbation at $At = 0$.

eventually to the optimal perturbation. Both direct and adjoint systems are integrated with the linearised version of the two-dimensional dealiased pseudo-spectral method used for the generation of the base flow. The outline is given in appendix B but the full description of the iterative optimisation algorithm is available in Lopez-Zazueta (2015). Practically, the convergence of this iterative optimisation algorithm is very quick since the solution is obtained most of the time in less than ten iterations.

A thorough validation of the numerical tool has been conducted in Lopez-Zazueta (2015) but we restrict it here to a short presentation of the optimal perturbation in the homogeneous case for a Reynolds number of $Re = 1000$ which corresponds to the work of Arratia *et al.* (2013). The figure 3 shows the optimal energy gain $\mathscr{G}_E$ obtained for various horizon times of a perturbation injected in the flow at $t_0 = 0$. The agreement with the results of Arratia *et al.* (2013) is excellent, see their figure 5.

2.4. *Diagnostics*

In order to understand the physical mechanisms associated with the energy growth of the optimal perturbations, it is useful to specify some diagnostics such as the evolution equation for the growth rate of the perturbation $\sigma_E = (1/E)\,\mathrm{d}E/\mathrm{d}t$. It is obtained straightforwardly from the transport equation for the perturbation kinetic energy $E = \|\boldsymbol{q}\|_u$ which reads

$$\begin{aligned}\frac{\mathrm{d}E}{\mathrm{d}t} = &\underbrace{-\iint u_x u_y \left(\frac{\partial U_x}{\partial y} + \frac{\partial U_y}{\partial x}\right)\mathrm{d}x\,\mathrm{d}y}_{\Pi_{E1}} + \underbrace{\frac{1}{2}\iint \left(u_x^2 - u_y^2\right)\left(\frac{\partial U_x}{\partial x} - \frac{\partial U_y}{\partial y}\right)\mathrm{d}x\,\mathrm{d}y}_{\Pi_{E2}} \\ &+ \underbrace{\iint \frac{1}{R}\left(u_x\frac{\partial p}{\partial x} + u_y\frac{\partial p}{\partial y} + u_z\frac{\partial p}{\partial z}\right)\mathrm{d}x\,\mathrm{d}y - \iint \frac{\rho}{R^2}\left(u_x\frac{\partial P}{\partial x} + u_y\frac{\partial P}{\partial y} + u_z\frac{\partial P}{\partial z}\right)\mathrm{d}x\,\mathrm{d}y}_{\Pi_{E3}} \\ &+ \underbrace{\frac{1}{2}\iint u_z^2\left(\frac{\partial U_x}{\partial x} + \frac{\partial U_y}{\partial y}\right)\mathrm{d}x\,\mathrm{d}y}_{\Pi_{E4}} + \underbrace{\frac{1}{Re}\iint \Phi_E\,\mathrm{d}x\,\mathrm{d}y}_{\Pi_{E\phi}},\end{aligned} \tag{2.15}$$

https://doi.org/10.1017/jfm.2016.509 Published online by Cambridge University Press

where Π_{E1} is the energy production/destruction by the base-flow shear, Π_{E2} the energy production/destruction by the base-flow strain field, Π_{E3} is the energy production/destruction coming form the coupling of density and pressure fields, Π_{E4} is the energy production/destruction by the base-flow dilatation/compression and $\Pi_{E\phi}$ is the viscous dissipation. Both Π_{E3} and Π_{E4} terms are specific to the variable-density situation and are not present in the homogeneous case, see equation (4.1) of Arratia *et al.* (2013). Π_{E3} corresponds to the remnant of the baroclinic vorticity production in the kinetic energy equation. For this reason, we will refer simply to it as the 'baroclinic' energy production hereinafter even if the semantic is not properly suited when dealing with the kinetic energy budget. Furthermore, because Π_{E4} is always very small, we chose to combine it with Π_{E2} in all the results presented in the paper.

Since the specificity of the variable-density flows considered here lies essentially in the baroclinic vorticity production, it is also useful to derive the linearised version of the vorticity equation (2.4) which writes

$$\frac{\partial \boldsymbol{\omega}}{\partial t} + \boldsymbol{U}\cdot\boldsymbol{\nabla}\boldsymbol{\omega} + \boldsymbol{u}\cdot\boldsymbol{\nabla}\boldsymbol{\Omega} = \boldsymbol{\Omega}\cdot\boldsymbol{\nabla}\boldsymbol{u} + \boldsymbol{\omega}\cdot\boldsymbol{\nabla}\boldsymbol{U} - \boldsymbol{\Omega}d - \boldsymbol{\omega}D + \boldsymbol{b} + \frac{1}{Re\,R}\left(\boldsymbol{\Delta}\boldsymbol{\omega} - \frac{\rho}{R}\boldsymbol{\Delta}\boldsymbol{\Omega}\right), \tag{2.16}$$

where $\boldsymbol{b}$ is the linearised baroclinic torque defined by

$$\boldsymbol{b} = \frac{1}{R}\boldsymbol{\nabla}R \times \underbrace{\left(\frac{1}{R}\boldsymbol{\nabla}p - \frac{\rho}{R^2}\boldsymbol{\nabla}P\right)}_{\text{(i)}} + \boldsymbol{\nabla}\left(\frac{\rho}{R}\right) \times \underbrace{\frac{1}{R}\boldsymbol{\nabla}P}_{\text{(ii)}}. \tag{2.17}$$

Pressure terms (i) and (ii) can be recast using an appropriate combination of the momentum equation for the base flow and for the perturbation. Given that $Re = 1000$, the viscous terms appearing in $\boldsymbol{b}$ are very small compared to the inertial terms and will be neglected in the following. Hence, the linearised baroclinic torque simplifies to

$$\boldsymbol{b} = -\frac{1}{R}\boldsymbol{\nabla}R \times \boldsymbol{a} - \boldsymbol{\nabla}\left(\frac{\rho}{R}\right) \times \boldsymbol{A}, \tag{2.18}$$

with $\boldsymbol{a}$ and $\boldsymbol{A}$ the linearised acceleration fields of the perturbation and the base flow respectively

$$\boldsymbol{a} = \frac{\partial \boldsymbol{u}}{\partial t} + \boldsymbol{U}\cdot\boldsymbol{\nabla}\boldsymbol{u} + \boldsymbol{u}\cdot\boldsymbol{\nabla}\boldsymbol{U}, \tag{2.19a}$$

$$\boldsymbol{A} = \frac{\partial \boldsymbol{U}}{\partial t} + \boldsymbol{U}\cdot\boldsymbol{\nabla}\boldsymbol{U}. \tag{2.19b}$$

From the vorticity transport equation (2.16), it is straightforward to derive an equation for the perturbation enstrophy $Z = \int\!\!\int \boldsymbol{\omega}^*\boldsymbol{\omega}\,\mathrm{d}x\,\mathrm{d}y$:

$$\frac{\mathrm{d}Z}{\mathrm{d}t} = \underbrace{\iint \omega_x\omega_y\left(\frac{\partial U_x}{\partial y} + \frac{\partial U_y}{\partial x}\right)\mathrm{d}x\,\mathrm{d}y}_{\Pi_{Z1}} + \underbrace{\frac{1}{2}\iint \left(\omega_x^2 - \omega_y^2\right)\left(\frac{\partial U_x}{\partial x} - \frac{\partial U_y}{\partial y}\right)\mathrm{d}x\,\mathrm{d}y}_{\Pi_{Z2}}$$
$$\underbrace{-\iint \omega_z\left(u_x\frac{\partial \Omega_z}{\partial x} + u_y\frac{\partial \Omega_z}{\partial y}\right)\mathrm{d}x\,\mathrm{d}y}_{\Pi_{Z3}} + \underbrace{\iint \Omega_z\left(\omega_x\frac{\partial u_x}{\partial z} + \omega_y\frac{\partial u_y}{\partial z} + \omega_z\frac{\partial u_z}{\partial z}\right)\mathrm{d}x\,\mathrm{d}y}_{\Pi_{Z4}}$$

https://doi.org/10.1017/jfm.2016.509 Published online by Cambridge University Press

$$\underbrace{-\frac{1}{2}\iint \omega_z^2\left(\frac{\partial U_x}{\partial x}+\frac{\partial U_y}{\partial y}\right)\mathrm{d}x\,\mathrm{d}y}_{\Pi_{Z5}}\underbrace{-\iint \omega_z\Omega_z\left(\frac{\partial u_x}{\partial x}+\frac{\partial u_y}{\partial y}+\frac{\partial u_z}{\partial z}\right)\mathrm{d}x\,\mathrm{d}y}_{\Pi_{Z6}}$$
$$+\underbrace{\iint(\omega_x b_x+\omega_y b_y+\omega_z b_z)\,\mathrm{d}x\,\mathrm{d}y}_{\Pi_{Z7}}+\underbrace{\frac{1}{Re}\iint \Phi_Z\,\mathrm{d}x\,\mathrm{d}y}_{\Pi_{Z\phi}}, \tag{2.20}$$

where Π_{Z1} is the enstrophy production/destruction by the base-flow shear, Π_{Z2} the enstrophy production/destruction by the base-flow strain field, Π_{Z3} is the enstrophy production/destruction by the base-flow spanwise vorticity advection by the perturbation, Π_{Z4} is the enstrophy production/destruction by vortex stretching, Π_{Z5} the enstrophy production/destruction by the base-flow dilatation/compression, Π_{Z6} the enstrophy production/destruction by dilatation/compression of the perturbation, Π_{Z7} the baroclinic enstrophy production/destruction and $\Pi_{Z\phi}$ is the viscous dissipation. The three terms Π_{Z5}, Π_{Z6} and Π_{Z7} are specific to the variable-density case. In the following of the paper, all terms that do not contribute significantly to the enstrophy budget will be gathered conveniently according to the cases considered.

3. Optimal perturbations in a high Atwood number mixing layer

3.1. *Optimal energy growth*

We first consider the optimal perturbations developing in the variable-density mixing layer when injected at the initial time of the development of the base flow, i.e. $t_0 = 0$. Figure 4 displays the optimal energy gain $\mathscr{G}_E$ as a function of the spanwise wavenumber k for different Atwood numbers and different horizon times ranging from $T = 10$ to $T = 60$. For short optimisation times ($T \lesssim 20$), the optimal energy growth is almost insensitive to the density variations since the curves in figure 4(*a*) are superimposed on each other. In that case, the interval of optimisation lies within the period of linear evolution of the primary KH wave during which the base flow remains quasi-parallel. When the horizon time is set equal to the saturation time of the primary KH mode ($T = t_{KH} = 30$), the optimal energy gain depends on the Atwood number as seen in figure 4(*b*). All amplification curves follow the same trend but the optimal energy gain is getting larger with increasing Atwood number. For optimisation times beyond t_{KH}, the influence of the Atwood number on the optimal energy growth is even more pronounced and the increase is not homogeneously spread amongst the spanwise wavenumbers. Optimal perturbations with large spanwise wavenumber benefit more from the variable-density effects than those with small spanwise wavenumber. This is readily observable in figure 4(*c*) for $T = 40$ but the difference is clear in figure 4(*d*) for $T = 60$. Despite this unequal gain enhancement, the overall maximum energy gain, associated with the so-called global optimal perturbation, always corresponds to a small spanwise wavenumber ($k < 1$), at least for the present moderate Reynolds number.

This difference in the increase of amplification is also observable in figure 5 where the temporal evolution of the energy gain is displayed until $t = 60$ for two perturbations optimised for $T = 40$. The first one is the global optimal which corresponds to a small spanwise wavenumber, $k = 0.6$ and the second one is a perturbation with a large wavenumber, $k = 4$. In the homogeneous case, they correspond respectively to perturbations leading to the development of an elliptic and a hyperbolic instability (Arratia *et al.* 2013). Just like these authors, we adopt

https://doi.org/10.1017/jfm.2016.509 Published online by Cambridge University Press

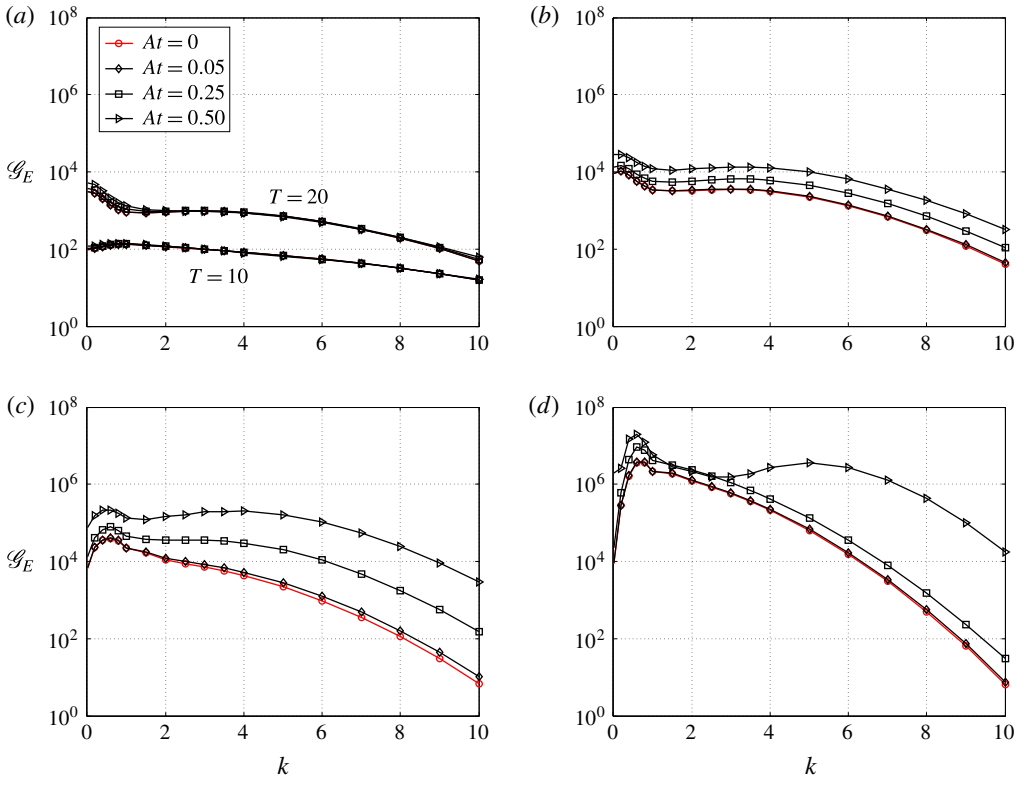


FIGURE 4. (Colour online) Influence of the Atwood number on the energy gain $\mathscr{G}_E$ as a function of the spanwise wavenumber k of the optimal perturbation for various horizon time: (*a*) $T = [10, 20]$, (*b*) $T = 30$, (*c*) $T = 40$ and (*d*) $T = 60$.

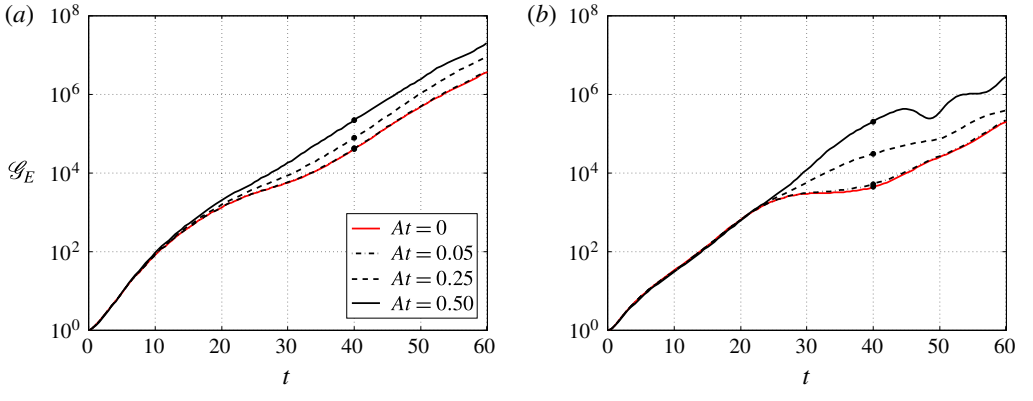


FIGURE 5. (Colour online) Temporal evolution of the optimal energy gain $\mathscr{G}_E$ for various Atwood numbers: optimal perturbation for $T = 40$ with (*a*) $k = 0.6$ and (*b*) $k = 4$. The bullet points denote the optimisation time.

https://doi.org/10.1017/jfm.2016.509 Published online by Cambridge University Press

the same terminology in the following of the paper: elliptical E-type and hyperbolic H-type perturbations will refer to optimal perturbations which develop respectively in the core and in the braid of the main structure. In agreement with the above observation, the initial evolution of their energy growth does not depend on the Atwood number. The influence of density variations is felt a little before $t = 20$ for the E-type perturbation while it starts a little after $t = 20$ for the H-type one. Hence, there are substantial changes in the base flow around that time which induce a significant modification of the optimal perturbation with increasing Atwood number. By $t = 20$, the baroclinic vorticity production has become substantial so that the vorticity field of the VDKH billow departs significantly from its homogeneous counterpart: the asymmetry of the vortex core as well as the intense layering of the stretched vorticity braid are distinctly observable, especially as the Atwood number is increased. For this reason we can introduce a bifurcation time, denoted $t_b \approx 20$, which clearly separates the evolution of the optimal perturbation into two periods provided that $T > t_b$: an initial one $[0, t_b]$ with a unique route for energy growth whatever the Atwood number, and a second one $[t_b, T]$ where density variations have a strong influence on the evolution of the optimal perturbation. In the following, we analyse each stage separately in order to identify the physical mechanisms at play in the growth of the optimal perturbation and elucidate the reason for this patent separation.

3.2. *First period* $[0, t_b]$

Figure 6 presents the early evolution of the field of the perturbation kinetic energy for the two same optimal perturbations considered in figure 5. The first and third columns correspond respectively to the evolution of perturbations in the homogeneous case at small and large wavenumbers: the E-type perturbation with $k = 0.6$, which is also the global optimal, and the H-type perturbation with $k = 4$. The second and fourth columns display their equivalent in the most density-contrasted case $At = 0.5$. For both types of perturbations and for homogeneous as well as for the inhomogeneous cases, the energy is initially concentrated in a thin layer centred around the hyperbolic braid saddle point and orientated along the direction of maximum compression of the base flow. When comparing both the homogeneous and the inhomogeneous cases, one can denote in the later a slight asymmetry of the energy field. The peak of energy is displaced towards the left side of the braid that will eventually roll-up into the billow on the light side of the mixing layer. This asymmetry anticipates the asymmetric development of the VDKH billow on the same pattern described in § 2.2. As the base flow evolves under the growth of the primary KH wave, the layers are progressively deformed under the action of the base-flow mean shear in such way so as to be realigned in the direction of the maximal stretching of the mixing layer. For the hyperbolic perturbation the energy stays concentrated in the braid region while for the elliptic one it progressively spreads out in the central zone where the core of the growing KH billow will be located.

The associated energy growth during this period is essentially due to base-flow shear conversion as can be seen in figure 7 which presents the temporal evolution of the energy growth rate budget according to equation (2.15) for the same four previous perturbations. By the end of the period around $t \sim 15$, the energy growth is also supplied by the base-flow strain conversion for the H-type perturbations. As expected from previous observations, the density variations have almost no influence on the kinetic energy budget during this period. For $At = 0.5$, the baroclinic term σ_{E3} remains close to zero and the other contributions to the growth rate do not differ

https://doi.org/10.1017/jfm.2016.509 Published online by Cambridge University Press

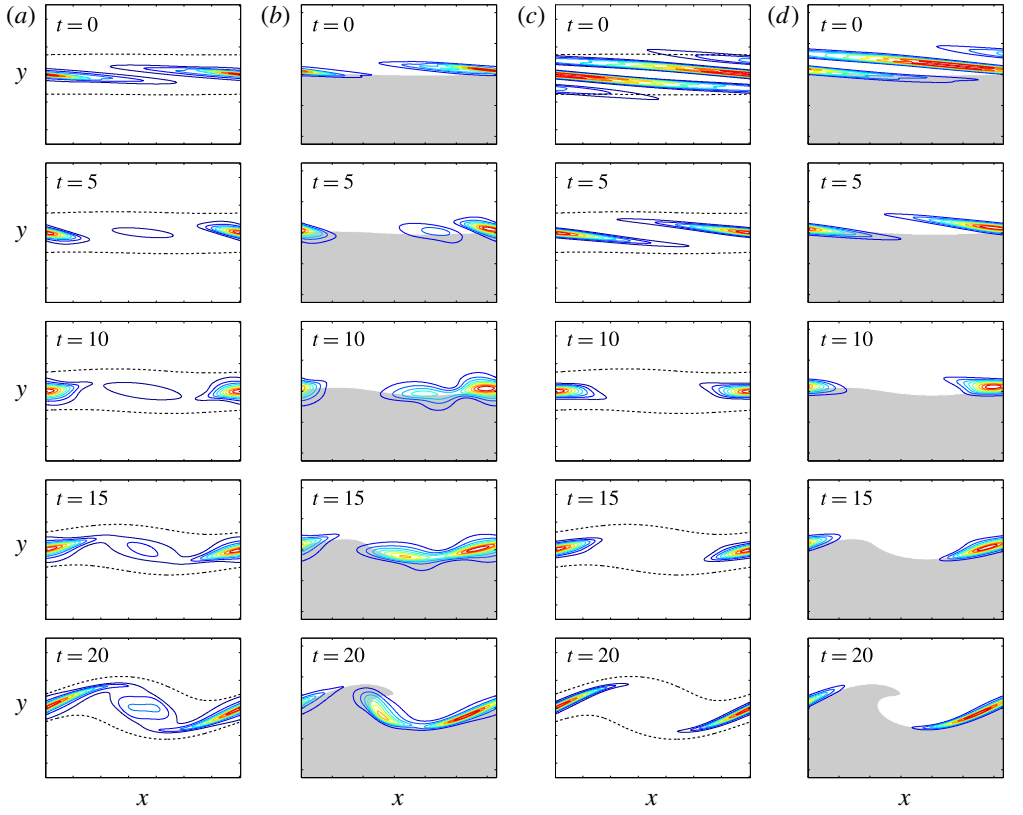


FIGURE 6. (Colour online) Temporal evolution of the energy field of the optimal perturbation during the time interval $[0, t_b]$. The perturbation is optimised for $T = 40$ with from (*a*) to (*d*): $At = 0, k = 0.6$ (*a*), $At = 0.5, k = 0.6$ (*b*), $At = 0, k = 4$ (*c*) and $At = 0.5, k = 4$ (*d*). In the homogeneous case, the dashed contour corresponds to 20 % of the maximal absolute value of the base-flow vorticity $|\Omega_m|$.

from the homogeneous case. This initial energy growth is due to the synergy of both classical Orr and lift-up transient mechanisms, as already observed by Arratia *et al.* (2013) in the homogeneous case. The Orr mechanism is associated with the kinematic deformation of initial spanwise vorticity patches under the action of the base-flow mean shear while the lift-up mechanism corresponds the emergence of longitudinal streaks of high and low velocity under the action of the base-flow mean shear onto an initial perturbation made of an array of longitudinal vortices. Hence, the relative contribution of each mechanism to the growth of the perturbation can be assessed through the ratio $f = \iint \omega_x^2(t_0)\,\mathrm{d}x\,\mathrm{d}y / \iint \omega_z^2(t_0)\,\mathrm{d}x\,\mathrm{d}y$ between the contribution of the longitudinal and the spanwise components of the vorticity to the perturbation enstrophy at the injection time. This quantity is displayed in figure 8 as a function of the spanwise wavenumber k and shows that E-type optimal perturbations ($f \lesssim 1$) are initially structured to take advantage of the Orr mechanism at low wavenumber while H-type ones ($f > 1$) are initially organised to benefit from the lift-up mechanism at higher wavenumbers.

https://doi.org/10.1017/jfm.2016.509 Published online by Cambridge University Press

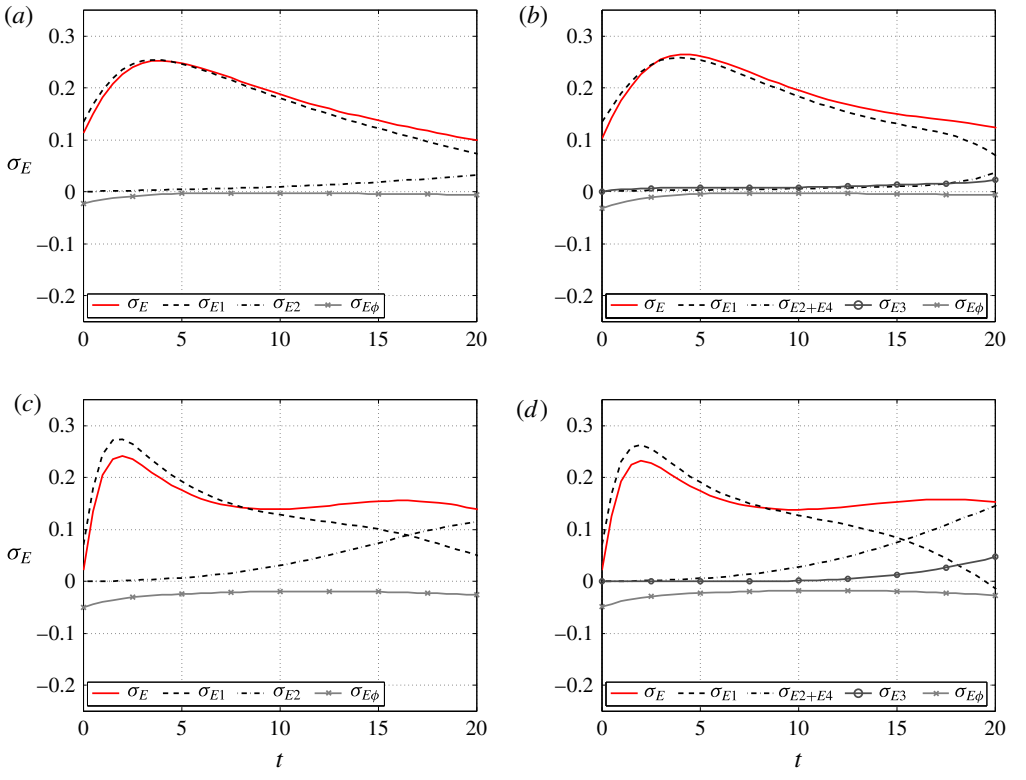


FIGURE 7. (Colour online) Temporal evolution of the kinetic energy growth rate σ_E and its different contributions for the optimal perturbation during the time interval $[t_0, t_b]$ according to equation (2.15). The perturbation is optimised for $T = 40$ with (*a*) $k = 0.6$, $At = 0$, (*b*) $k = 0.6$, $At = 0.5$, (*c*) $k = 4$, $At = 0$ and (*d*) $k = 4$, $At = 0.5$.

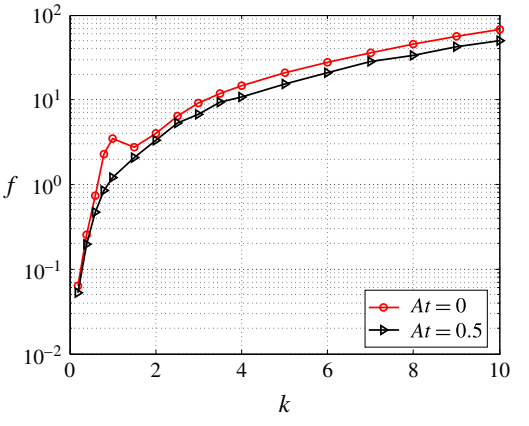


FIGURE 8. (Colour online) Initial ratio between the contribution to enstrophy of the longitudinal and the spanwise components of the vorticity $f = \int\int \omega_x^2(t_0)\,\mathrm{d}x\,\mathrm{d}y / \int\int \omega_z^2(t_0)\,\mathrm{d}x\,\mathrm{d}y$ as a function of the spanwise wavenumber k of the optimal perturbation optimised at $T = 40$ for $At = 0$ and $At = 0.5$.

https://doi.org/10.1017/jfm.2016.509 Published online by Cambridge University Press

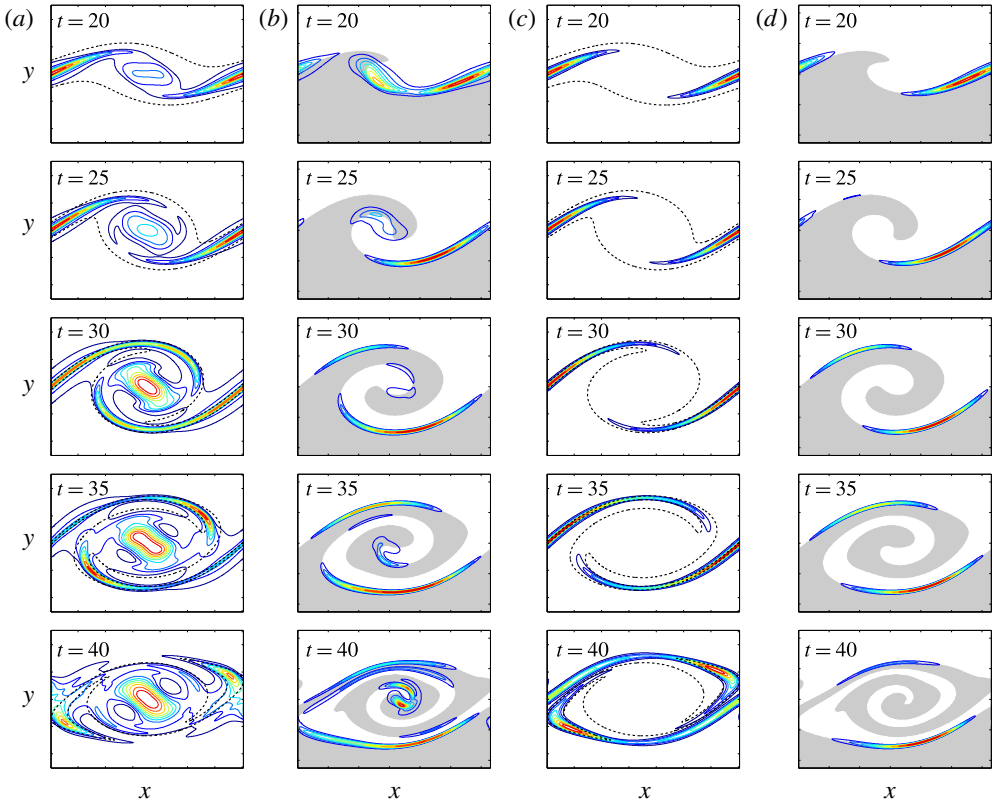


FIGURE 9. (Colour online) Temporal evolution of the energy field of the optimal perturbation during the time interval $[t_b, T]$. The perturbation is optimised for $T = 40$ with $At = 0$, $k = 0.6$ (a), $At = 0.5$, $k = 0.6$ (b), $At = 0$, $k = 4$ (c) and $At = 0.5$, $k = 4$ (d).

3.3. *Second period* $[t_b, T]$

We now focus on the second period of the development of the optimal perturbations after the bifurcation time. At this stage, the influence of the Atwood number is substantial as can be seen from figure 9 where the structure of the perturbations at $At = 0.5$ departs clearly from the homogeneous case. As for the perturbation with a small wavenumber, the energy concentrates essentially into two asymmetric thin layers located along the braid of the VDKH billow. This asymmetry between the layers is imposed by the asymmetric development of the primary roll-up discussed in § 2.2. Even if some small amount of energy still lies within the core of the primary structure, most of it is concentrated within the two thin layers located along the braid. This pattern is not comparable to the one observed in the homogeneous case. We conclude that the perturbation cannot be labelled as an E-type perturbation anymore but that it is rather an H-type one as it concentrates in the braid region. This change in the nature of the perturbation is not that surprising if one refers to the results of the modal analysis of Fontane & Joly (2008) performed at the saturation time of the primary wave. It was found that the growth rate σ_r of the elliptic modes were insensitive to the increase of the Atwood number while the hyperbolic ones were strongly enhanced by density effects. In the (k, σ_r) plane, this resulted in the progressive drift of the elliptic modes towards the group of weakly amplified modes

https://doi.org/10.1017/jfm.2016.509 Published online by Cambridge University Press

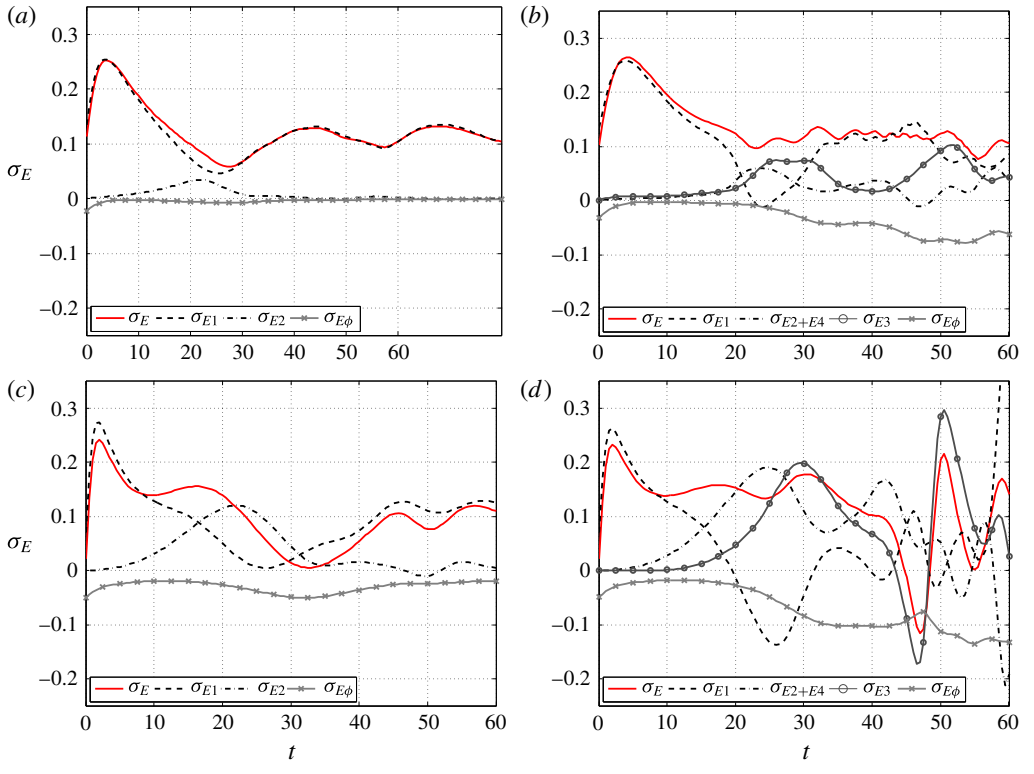


FIGURE 10. (Colour online) Temporal evolution of the kinetic energy growth rate σ_E and its different contributions for the optimal perturbation during the time interval $[t_0, 60]$ according to equation (2.15). The perturbation is optimised for $T = 40$ with (*a*) $k = 0.6$, $At = 0$, (*b*) $k = 0.6$, $At = 0.5$, (*c*) $k = 4$, $At = 0$ and (*d*) $k = 4$, $At = 0.5$.

so that they could not even be identified with the modal analysis at $At = 0.5$ (see figure 4 of Fontane & Joly 2008). Hence, the computation of several sub-optimal perturbations (not performed here) would be required in order to exhibit an E-type perturbation at $k = 0.6$. On the other hand, the large wavenumber perturbation is developing on a similar pattern than the small wavenumber one but with no energy located within the core of the VDKH billow. It remains clearly an H-type perturbation.

Figure 10 displays the temporal evolution of the kinetic energy growth rate σ_E and its different contributions according to equation (2.15). In the homogeneous case, nearly all the energy of the E-type perturbation at $k = 0.6$ comes from the base-flow shear conversion σ_{E1} as already observed by Arratia *et al.* (2013) (see their figure 7). In the density-contrasted situation, this term still provides the largest contribution to the energy growth throughout the optimisation period but both the baroclinic term σ_{E3} and the base-flow strain conversion σ_{E2} contribute significantly to the growth of the perturbation after the bifurcation time. For large wavenumbers, the H-type perturbation at $k = 4$ in the homogeneous case extracts energy from the base flow alternatively through the shear σ_{E1} and strain σ_{E2} terms, in agreement with Arratia *et al.* (2013). In the inhomogeneous case, the picture is more complex with a combined contribution of all terms of the equation (2.15), none of them being predominant and each one turning intermittently into a sink term during the time interval. One can also notice

https://doi.org/10.1017/jfm.2016.509 Published online by Cambridge University Press

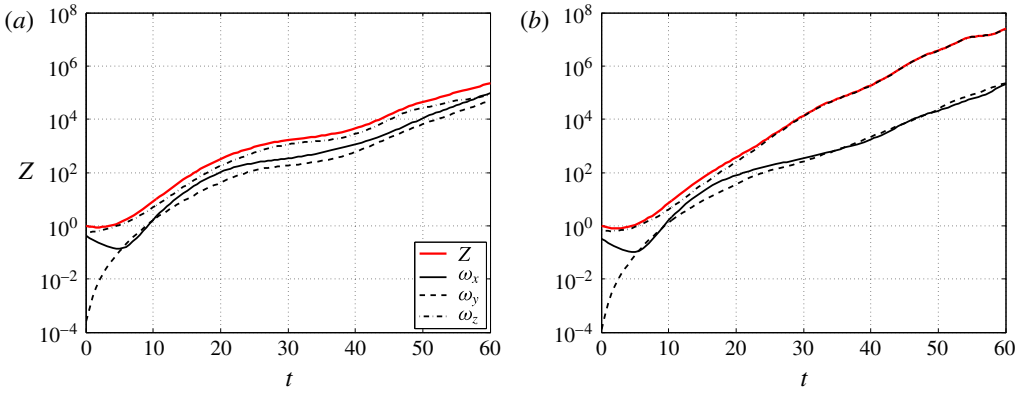


FIGURE 11. (Colour online) Temporal evolution of the enstrophy Z and the relative contribution of each vorticity component ω_x, ω_y and ω_z for the global optimal perturbation during the time interval $[t_0, 60]$. The perturbation is optimised for $T = 40$ with (*a*) $At = 0$ and (*b*) $At = 0.5$.

that both small and large wavenumber perturbations share a common feature in the variable-density case. After the bifurcation time t_b, there is a substantial increase of the dissipation term $\sigma_{E\phi}$ compared to their homogeneous counterparts. This is related to the structuring of the optimal perturbation on thin layers associated with larger gradients yielding enhanced viscous dissipation.

This detailed analysis of the perturbation kinetic energy budget only enables us to identify major contributions to the perturbation growth but fails at giving an understanding of the physical mechanisms associated with the observed extra energy growth. As mentioned previously in § 2, the specificity of these variable-density flows compared to their homogeneous counterparts is best understood from their vorticity dynamics. Thus, we now examine carefully the perturbation enstrophy budget and we focus first on the global optimal perturbation corresponding to small spanwise wavenumber before considering optimal perturbations with larger k.

Figure 11 shows the temporal evolution of the enstrophy Z of the global optimal at $At = 0$ and $At = 0.5$ together with the relative contribution of each vorticity component. Not only the enstrophy growth in the variable-density case is enhanced after the bifurcation time but it is also clearly due to the growth of spanwise vorticity component ω_z when all vorticity components contribute equally in the homogeneous case. Considering the temporal evolution of the enstrophy growth rate σ_Z and its different contributions according to equation (2.20) plotted in figure 12, one can see that the main difference lies in the substantial increase of the baroclinic vorticity production σ_{Z7}. It onsets around the bifurcation time and remains the main source of enstrophy together with the advection term σ_{Z3}, already active in the homogeneous case. The base-flow shear conversion term σ_{Z1}, which provides the main contribution to the enstrophy growth during the first period $[t_0, t_b]$, quickly goes to zero after the bifurcation time while it remains a significant source of enstrophy in the homogeneous case. As observed for the kinetic energy, the variable-density effects are also responsible for a significant increase of the enstrophy dissipation owing to the development of small scales and to the layered structure of the perturbation vorticity field (see figure 14*b*). The extra dissipation is overcompensated by a larger increase of the σ_{Z3} term after t_b yielding larger growth.

https://doi.org/10.1017/jfm.2016.509 Published online by Cambridge University Press

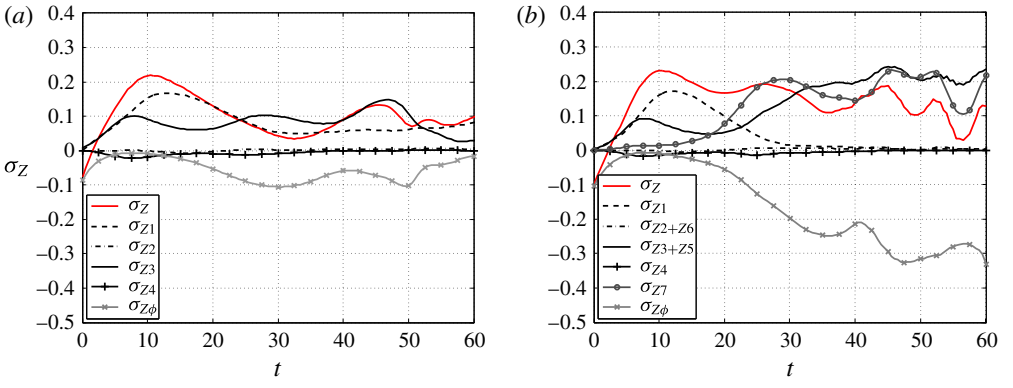


FIGURE 12. (Colour online) Temporal evolution of the enstrophy growth rate σ_Z and its different contributions for the global optimal perturbation during the time interval $[t_0, 60]$ according to equation (2.20). The perturbation is optimised for $T = 40$ with (*a*) $At = 0$ and (*b*) $At = 0.5$.

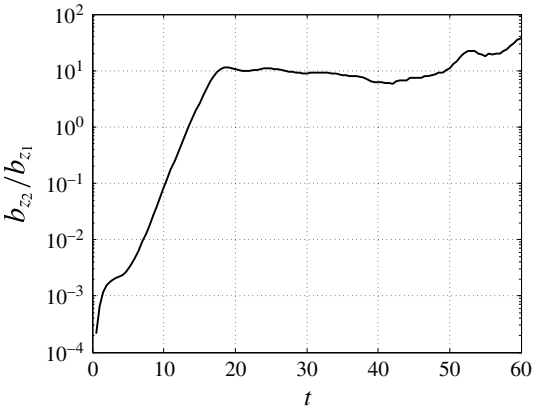


FIGURE 13. Temporal evolution of the ratio between the two terms constituting the spanwise component of the linearised baroclinic torque (3.1). The perturbation is optimised for $T = 40$ with $k = 0.6$ and $At = 0.5$.

We now analyse in detail the contribution of the baroclinic torque to the growth of the optimal perturbation. The spanwise component b_z of the linearised baroclinic torque (2.17) comes as the sum of two contributions:

$$b_z = \underbrace{a_x \frac{1}{R}\frac{\partial R}{\partial y} - a_y \frac{1}{R}\frac{\partial R}{\partial x}}_{b_{z_1}} + \underbrace{A_x \frac{\partial}{\partial y}\left(\frac{\rho}{R}\right) - A_y \frac{\partial}{\partial x}\left(\frac{\rho}{R}\right)}_{b_{z_2}}. \tag{3.1}$$

The first term b_{z_1} corresponds to the cross-product between the acceleration of the perturbation and the base-flow density field while the second one b_{z_2} is the cross-product between the acceleration of the base flow and the perturbation density field. The temporal evolution of the ratio between both terms b_{z_2}/b_{z_1} is plotted in figure 13. The term b_{z_2} becomes predominant a little before t_b by an order of

https://doi.org/10.1017/jfm.2016.509 Published online by Cambridge University Press

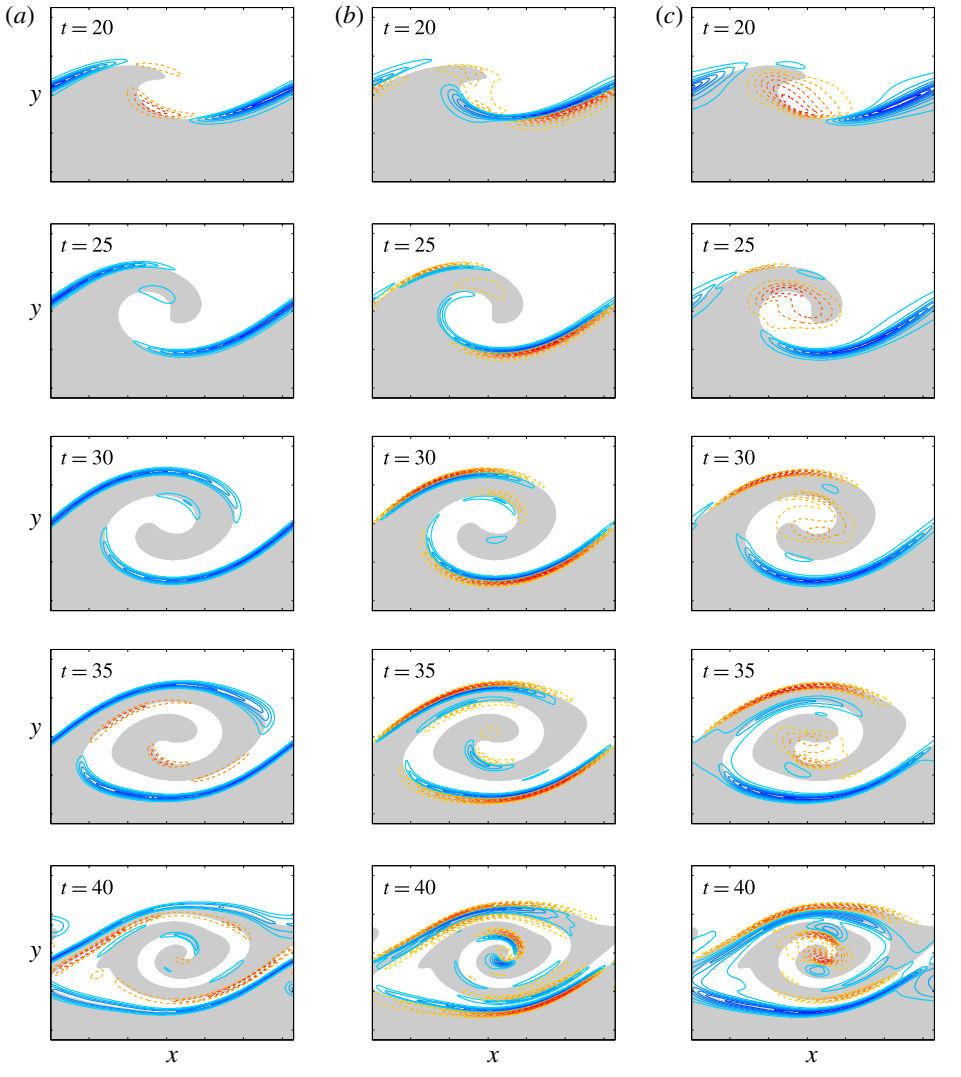


FIGURE 14. (Colour online) Temporal evolution of density ρ (a), spanwise vorticity ω_z (b) and longitudinal velocity u_x (c) of the global optimal perturbation during the time interval $[t_b, T]$. The perturbation is optimised for $T = 40$ with $At = 0.5$.

magnitude and is responsible for the substantial increase of the spanwise perturbation vorticity. Looking at the evolution of the perturbation density field during the interval $[t_b, T]$ in figure 14(a), it is mainly structured in a thin layer of negative density located along the braid. Combined with the two-dimensional base-flow acceleration field in the hyperbolic braid region, it results in a contribution of term b_{z_2} organised into a quadrupole centred on the braid saddle point S as sketched in figure 15 for $t = 25$. This distribution is consistent with the contribution of the linear baroclinic torque b_z also plotted in figure 15. At the bifurcation time, the spanwise perturbation vorticity ω_z consists of two elongated layers of opposite sign along the braid as can be seen in figure 14(b). In the half of the braid located on the left side of the saddle point, the baroclinic torque contributions are of the same sign as the current perturbation

https://doi.org/10.1017/jfm.2016.509 Published online by Cambridge University Press

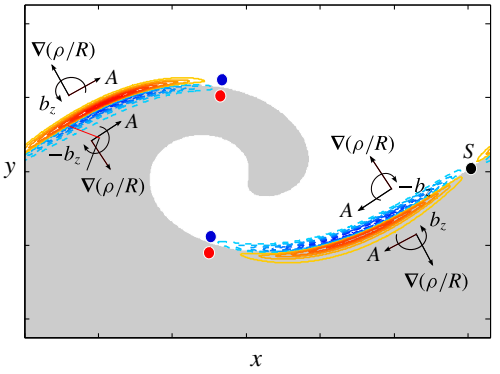


FIGURE 15. (Colour online) Spanwise component of the linear baroclinic torque b_z at $t = 25$ for the global optimal perturbation together with a schematic representation of the contribution of term b_{z_2} sketched on top of it. Red and blue dots indicate the local sign of the spanwise vorticity of the perturbation before the action of the baroclinic torque at time t_b.

spanwise vorticity indicated by the coloured bullet points in figure 15. Thus, they locally enhance the two existing layers of perturbation vorticity. Conversely, in the half of the braid located on the right side of the saddle point, the two spanwise baroclinic production terms are of opposite sign to the one of the local vorticity field and contribute to its destruction. As displayed in figure 14(*b*), the spanwise vorticity layers in the right-upper part of the braid are quickly cancelled under the action of the baroclinic torque before being replaced by two layers of opposite sign which are readily observable at $t = 25$. By $t = 30$, the spanwise vorticity field of the perturbation is structured on each side of the saddle point into two elongated layers of opposite sign according to spanwise vorticity baroclinic production. This pattern of elongated opposite shear layers is characteristic of longitudinal jets which is confirmed by looking at the perturbation longitudinal velocity field u_x in the third column of figure 14(*c*). At $t = 30$, it consists of two streaks of opposite sign located along the braid on either side of the saddle point. These streaks are responsible for the essential of the perturbation energy growth as shown in figure 16. While the contribution of each component of the velocity to the energy gain is isotropic in the homogeneous case, the energy growth is primarily due to the increase of the perturbation longitudinal velocity component in the variable-density case. This is corroborated by a similar evolution of the structure for both the longitudinal velocity field and the energy field in figures 14(*c*) and 9.

The physical mechanism for energy growth described previously is generic for all optimal perturbations identified here whatever the value of the spanwise wavenumber. For larger wavenumber, the enstrophy and energy growth are also driven by the increase of the spanwise vorticity and longitudinal velocity respectively as illustrated in figure 17 for $k = 4$. The enstrophy budget in figure 18 attests that extra enstrophy growth is again related to the onset of the baroclinic vorticity production σ_{Z7}. The main difference with the small wavenumber optimal perturbation is the contribution to the enstrophy growth of the base-flow strain conversion term σ_{Z2}, which is already active in the homogeneous case. The same structure for the perturbation density field consisting of a thin layer located along the braid (figure 19*a*) results in a similar quadrupolar pattern for the spanwise baroclinic torque (figure 19*b*). It yields

https://doi.org/10.1017/jfm.2016.509 Published online by Cambridge University Press

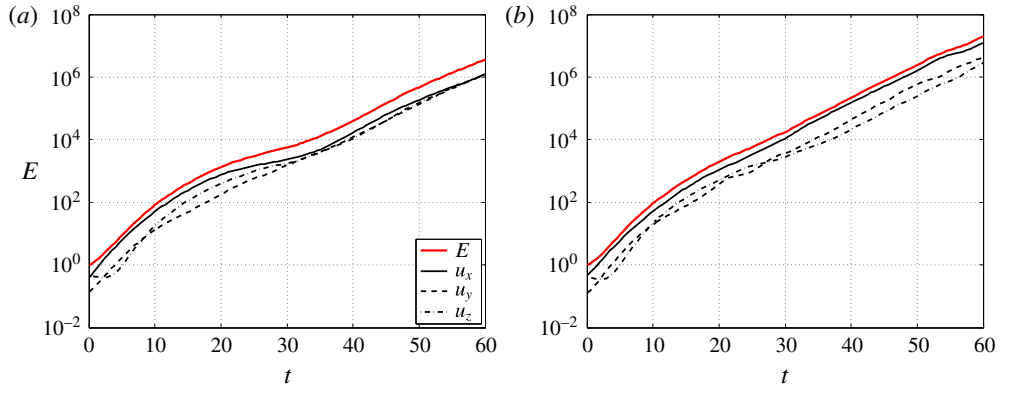


FIGURE 16. (Colour online) Temporal evolution of the energy E and the relative contribution of each velocity component u_x, u_y and u_z for the global optimal perturbation during the time interval $[t_0, 60]$. The perturbation is optimised for $T = 40$ with (*a*) $At = 0$ and (*b*) $At = 0.5$.

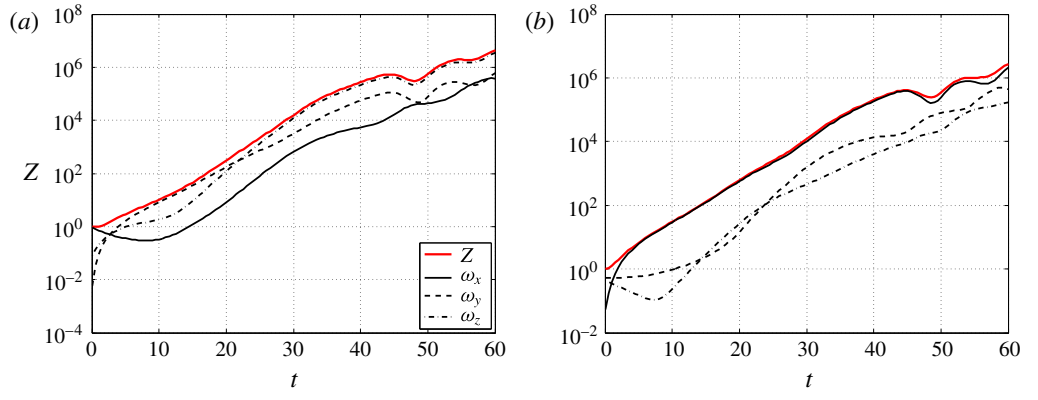


FIGURE 17. (Colour online) Temporal evolution of (*a*) the enstrophy Z and the relative contribution of each vorticity component ω_x, ω_y and ω_z and (*b*) the energy E and the relative contribution of each velocity component u_x, u_y and u_z for the optimal perturbation with $k = 4$ during the time interval $[t_0, 60]$. The perturbation is optimised for $T = 40$ with $At = 0.5$.

to the production of two thin layers of spanwise vorticity along the braid on either side of the saddle point (figure 19*c*) which eventually give rise to the longitudinal velocity streaks (figure 19*d*) responsible for the optimal energy growth (figure 17*b*). Comparing figures 14 and 19, the sign difference between the perturbation fields only comes from the arbitrary phase associated with the z-planes at which the fields are represented.

The optimal mechanism for energy growth elucidated here relies on the emergence on either side of the saddle point of longitudinal velocity streaks of opposite sign along the baroclinically enhanced vorticity braid of the primary VDKH billow. Figure 20 gives a three-dimensional view of this transitional scenario which differs completely from the promotion of rib vortices along the braid observed in the homogeneous case (Arratia *et al.* 2013) and so far accepted as the paradigm for

https://doi.org/10.1017/jfm.2016.509 Published online by Cambridge University Press

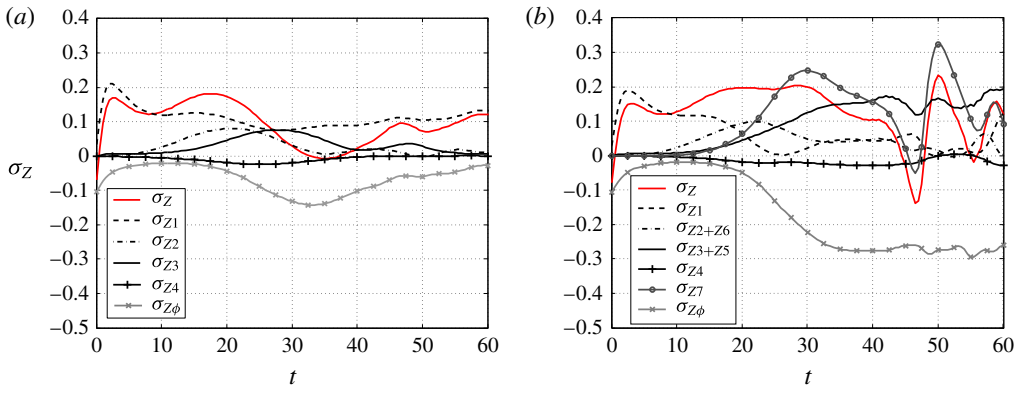


FIGURE 18. (Colour online) Temporal evolution of the enstrophy growth rate σ_Z and its different contributions for the optimal perturbation with $k = 4$ during the time interval $[t_0, 60]$ according to equation (2.20). The perturbation is optimised for $T = 40$ with (*a*) $At = 0$ and (*b*) $At = 0.5$.

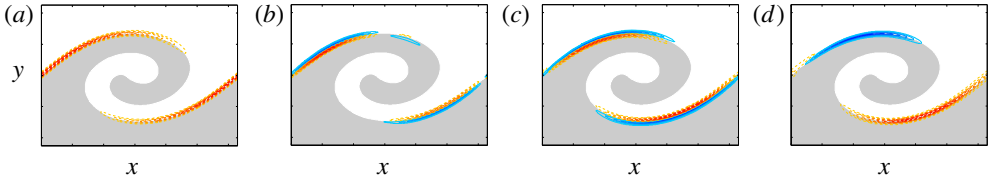


FIGURE 19. (Colour online) (*a*) Density ρ, (*b*) spanwise baroclinic torque b_z, (*c*) spanwise vorticity ω_z and (*d*) longitudinal velocity u_x fields of the optimal perturbation at $t = 30$. The perturbation is optimised for $T = 40$ with $k = 4$ and $At = 0.5$.

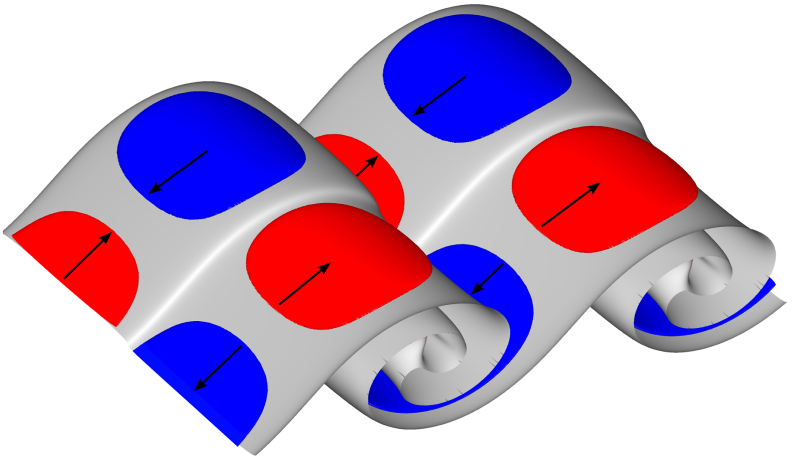


FIGURE 20. (Colour online) Illustration of the three-dimensionalisation process of variable-density free shear layers in the case of the global optimal perturbation at $t = 30$ with $k = 0.6$, $T = 40$ and $At = 0.5$. The grey surface corresponds to mean isopycnal of the perturbed VDKH billow. The red and blue regions denote the positive and negative longitudinal velocity streaks associated with the optimal perturbation at the same time, also indicated by the arrows. They correspond respectively to values of $0.2u_{x,max}$ and $0.2u_{x,min}$.

https://doi.org/10.1017/jfm.2016.509 Published online by Cambridge University Press

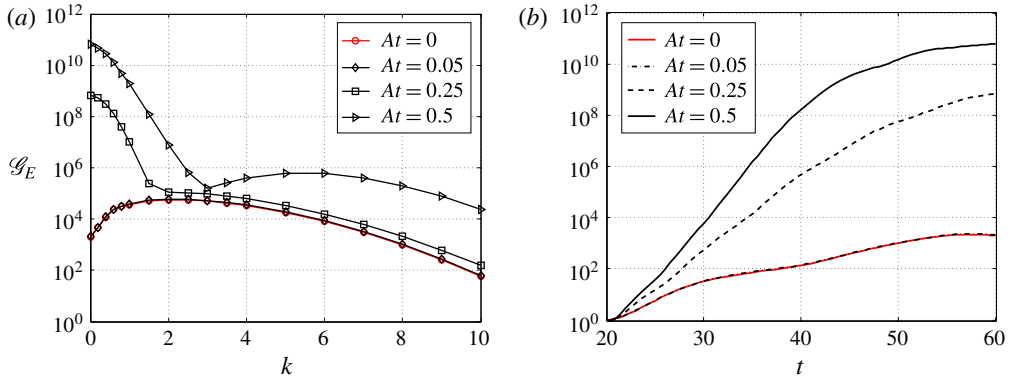


FIGURE 21. (Colour online) (*a*) Influence of the Atwood number on the energy gain $\mathscr{G}_E$ as a function of the spanwise wavenumber k of the optimal perturbations in the interval $[t_0, T] = [20, 60]$. (*b*) Temporal evolution in the interval $[t_0, T] = [20, 60]$ of the energy gain $\mathscr{G}_E$ for the optimal perturbation with $k = 0$ and various Atwood numbers.

three-dimensionalisation of free shear flows. If the route to three-dimensionalisation identified here is generic to all variable-density free shear flows, it calls into question the physical mechanism originally advocated by Monkewitz & Pfizenmaier (1991) and extended by Brancher *et al.* (1994) for the generation of the side jets occurring in light round jets. These authors claimed that the emergence of side jets relies on the velocity induction by the pairs of counter-rotating streamwise vortices associated with the secondary three-dimensional instabilities. The present analysis rather suggests that a more likely mechanism for side ejections would be based on the convergence of the two longitudinal velocity streaks of opposite sign near the braid saddle point. Although quite plausible, this conjecture must be examined further before being asserted. It would be interesting to look first at the three-dimensional nonlinear development of the optimal perturbation and scrutinise the velocity field in the crosswise plane located at the saddle point. Second, a similar non-modal analysis performed for round jets would confirm if this original route to three-dimensional motions is robust to the axisymmetrisation of the plane KH-rollers into a vortex ring. These perspectives are beyond the scope of the present study and are left to future work.

3.4. *Influence of the injection time*

Until this point the perturbations were optimised for a given horizon time T by being injected in the flow at the initial time of the base-flow evolution, i.e. $t_0 = 0$. The influence of the Atwood number on the energy growth of optimal perturbations has been found to be negligible during the initial period $[0, t_b]$ where the energy growth is due to a combination of the Orr and lift-up mechanisms. We probe the influence of the injection time t_0 setting the injection time as $t_0 = t_b = 20$ in order to skip the initial period of growth and see how it affects the evolution of the optimal perturbations.

The figure 21 presents the energy gain $\mathscr{G}_E$ as a function of the spanwise wavenumber k and various Atwood numbers for the perturbations optimised during the interval $[t_0, T] = [20, 60]$. In the homogeneous case, as already observed by Arratia *et al.* (2013), the energy gain is reduced for all the spanwise wavenumbers except for the very large ones ($k \gtrsim 8$) where a slight increase of the gain can be noticed

https://doi.org/10.1017/jfm.2016.509 Published online by Cambridge University Press

when comparing figures 4(*d*) and 21(*a*). The reduction in energy gain, which is even more pronounced for perturbations with small wavenumber, is due to the shortening of the initial period during which the Orr and lift-up mechanisms are the most effective. Nevertheless, all the optimal perturbations still undergo a short initial phase of transient growth before evolving towards the elliptic and hyperbolic modes (Arratia *et al.* 2013). In the variable-density case, the picture is very different and displays a discontinuity in the curves for a given wavenumber k_c which denotes the coexistence of two distinct branches corresponding to optimal perturbations of different nature. The spanwise wavenumber k_c at which the two branches cross increases with the Atwood number. We measure $k_c \approx 1.7$ and $k_c \approx 2.8$ respectively for $At = 0.25$ and $At = 0.5$. The perturbations of the first branch, corresponding to small spanwise wavenumbers, exhibit energy gain significantly larger than those of the second branch spanning the large wavenumbers. The largest gain of the first branch, which is also the overall maximum, corresponds to a two-dimensional perturbation, i.e. $k = 0$. It is also significantly higher than those observed in § 3.1. This strongly suggests that the optimal perturbation is of a very different nature from the one obtained for similar wavenumbers when the optimisation started from $t_0 = 0$. Conversely, the second branch presents a maximum located around $k \approx 5.5$ and a shape which is very close to what was obtained for an optimisation from $t_0 = 0$, indicating that the nature of the perturbation is likely to be the same for this range of wavenumbers.

To determine the nature and identify the physical mechanisms of energy growth behind the perturbation of the first branch, we analyse in detail the characteristics of the two-dimensional global optimal. The effect of the Atwood number on the evolution of the energy gain $\mathscr{G}_E$ is displayed in figure 21(*b*). It is remarkable to note that the perturbation reaches quickly energy levels much higher than those measured in homogeneous situation. By $t = 25$, the gain measured for $At = 0.5$ is already twice the one obtained for $At = 0$. At the time horizon T, the energy gain is respectively five and seven orders of magnitude higher for $At = 0.25$ and $At = 0.5$ respectively. The structure of the optimal perturbation consists of small elongated spanwise vorticity patches of alternate sign located along the braid on the left side of the saddle point as displayed in figure 22 at $t = 20$. As the primary KH wave overturns, the patches deform and move progressively towards the core of the VDKH billow following the central isopycnal $\rho = \rho_0$. This perturbation corresponds to the secondary KH instability of the baroclinically enhanced vorticity braid identified in the modal stability analysis of Fontane & Joly (2008) and originally discovered by Reinaud *et al.* (2000).

The evolution of the perturbation can be decomposed into three stages when considering the temporal evolution of both the energy and enstrophy growth rate budgets in figure 23. The early initial energy growth, $20 \leqslant t \lesssim 22$, of the two-dimensional optimal perturbation is due to the Orr mechanism. As shown in figure 22, at the injection time $t_0 = 20$, the vorticity patches are orientated in the direction corresponding locally to the maximal compression of the stretched braid. Then, while being convected towards the core of the VDKH billow, the patches are immediately tilted into the direction of the local maximal stretching under the action of the base-flow shear. During this kinematic deformation, the perturbation extracts energy from base-flow shear conversion relying on the Orr mechanism. This is confirmed in figure 23(*a*) where one can see a strong increase of the σ_{E1} term which is the main contribution to the energy growth during this initial period. This transient contribution reaches its maximum around $t \sim 22$ before decreasing quickly.

The second stage of evolution, $22 \lesssim t \lesssim 30$, is characterised by an intense baroclinic production of vorticity as denoted by the sudden increase of term σ_{Z7} in figure 23(*b*)

https://doi.org/10.1017/jfm.2016.509 Published online by Cambridge University Press

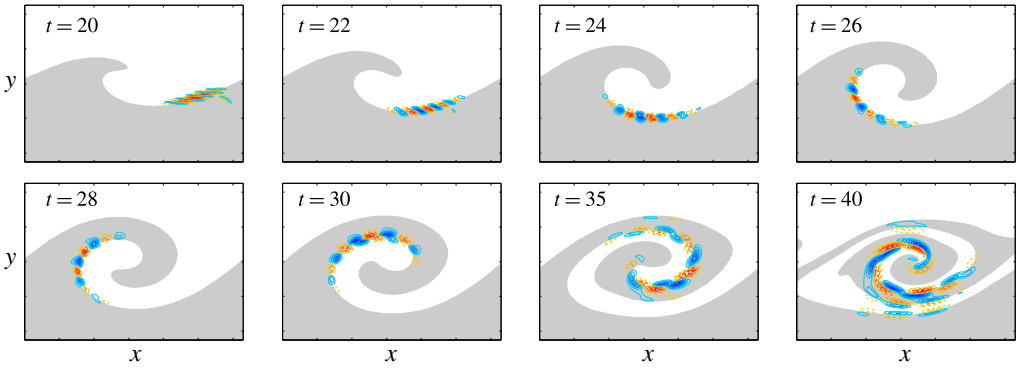


FIGURE 22. (Colour online) Temporal evolution of the spanwise vorticity field ω_z for the global optimal perturbation during the time interval $[t_0, 40]$. The perturbation is optimised for $t_0 = 20$ and $T = 60$ with $k = 0$ and $At = 0.5$.

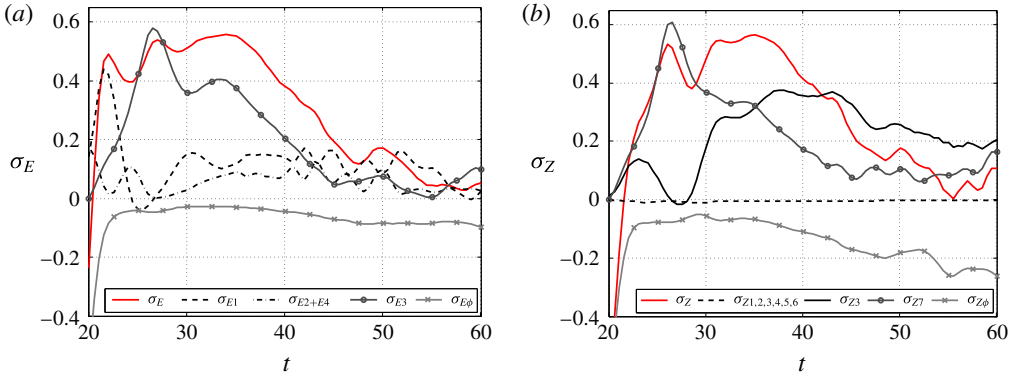


FIGURE 23. (Colour online) Temporal evolution of (*a*) the kinetic energy growth rate σ_E according to equation (2.15) and (*b*) the enstrophy growth rate σ_Z according to equation (2.20) for the perturbation optimised during the interval $t = [20, 60]$ with $k = 0$ and $At = 0.5$.

which becomes the main contributor to the perturbation enstrophy growth. It is worth noting that the enstrophy budget simply relies on the balance between three terms throughout the perturbation evolution: the term σ_{Z3} of production by base-flow spanwise vorticity advection by the perturbation, the baroclinic production σ_{Z7} and the viscous dissipation $\sigma_{Z\phi}$. During this stage, the vorticity production is very intense because the structure of the spanwise baroclinic torque presents a distribution of alternated sources and sinks that closely matches the perturbation spanwise vorticity field as can be seen in figure 24. This baroclinic production of vorticity is directly connected to the energy growth of the perturbation via the term of energy production σ_{E3} which prevails over other source terms and allows the perturbation to keep on growing once the Orr mechanism is stopped, see figure 23(*a*). By $t = 30$, the pattern of the vorticity patches is similar to that associated with the classic KH shear instability.

After $t \gtrsim 30$, the baroclinic contribution σ_{E3} to the energy growth decreases down to levels equivalent to the other sources terms of shear conversion σ_{E1} and of strain

https://doi.org/10.1017/jfm.2016.509 Published online by Cambridge University Press

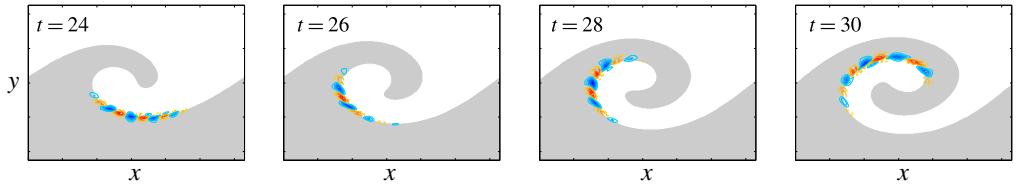


FIGURE 24. (Colour online) Temporal evolution of the spanwise component of baroclinic torque b_z for the global optimal perturbation during the time interval [24, 30]. The perturbation is optimised for $t_0 = 20$ and $T = 60$ with $k = 0$ and $At = 0.5$.

conversion σ_{E2}. The energy growth rate of the perturbation decreases consequently and from $t \sim 40$, the energy growth of the perturbation is slowed down significantly (see figure 21(*b*)) due to the combined decrease of σ_{E3} term and a slight increase of the viscous dissipation $\sigma_{E\phi}$. By the end of the optimisation interval, the energy growth rate is close to zero and the energy gain $\mathscr{G}_E$ plateaus, see figure 21(*b*).

The emergence of this secondary two-dimensional KH instability relies on the base-flow baroclinic vorticity production in the braid. As demonstrated by Dritschel *et al.* (1991), the instability can onset only if the local amount of vorticity is high enough to overcome the stabilising effect of the local stretching field in the braid. For this reason, the instability is not observed in homogeneous mixing layers where the magnitude of the vorticity field in the braids is too weak. As shown by Reinaud *et al.* (2000) and Fontane & Joly (2008), the nonlinear development of this type of instability leads to the formation of smaller secondary vortical structures similar to the primary VDKH billow, opening the way to a cascade of two-dimensional KH rollers of smaller and smaller size (Fontane, Joly & Reinaud 2008). This unlikely two-dimensional transition to turbulence is radically different from both the one relying on homogeneous rib vortices or the one relying on the longitudinal velocity streaks, as found in the previous section for the variable-density case. Compared to the modal analysis of Fontane & Joly (2008), the present work allows us to discuss a little further the competition between the two scenarios identified in the variable-density case. The secondary KH perturbation being only observed when the injection time is delayed, it is likely that the development of three-dimensional hyperbolic modes from the initial time of the flow evolution would preclude a purely two-dimensional scenario in natural variable-density mixing layers. Besides, the two-dimensional secondary KH mode has not been observed experimentally so far. Nevertheless, additional calculations displayed in figure 25, show that the two-dimensional optimal perturbation becomes the global optimal for $At = 0.5$ when the injection time is as small as $t_0 = 10$. Turning towards spatially developing mixing layers, the experimental evidence of such a striking two-dimensional response may require to delay the two-dimensional forcing at some distance downstream the splitter plate. Such an experiment is not straightforward and would certainly require a complex and very challenging experimental set-up.

The optimal perturbations of the second branch correspond to development of the same three-dimensional hyperbolic modes observed when the injection time is $t_0 = 0$. They follow the same physical mechanism described in § 3.3 leading to the emergence of the longitudinal velocity streaks in the braid region. A further description of these perturbations would not bring any new information and is thus not necessary at this point.

https://doi.org/10.1017/jfm.2016.509 Published online by Cambridge University Press

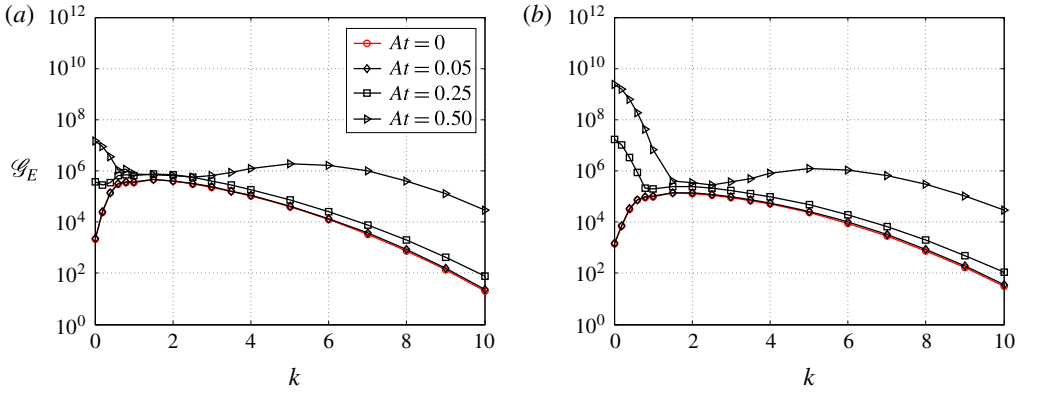


FIGURE 25. (Colour online) Influence of the Atwood number on the energy gain $\mathscr{G}_E$ as a function of the spanwise wavenumber k of the optimal perturbations in the interval (*a*) $[t_0, T] = [10, 60]$ and (*b*) $[t_0, T] = [15, 60]$.

4. Conclusions

The present work aims at determining the three-dimensional perturbations maximising their kinetic energy growth when developing over a time-dependent variable-density mixing layer undergoing the primary KH instability. Direct numerical simulations are carried out to obtain the temporal evolution of the two-dimensional variable-density KH billows. The Reynolds and Schmidt numbers are fixed to $Re = 1000$ and $Sc = 1$ respectively while the Atwood number is varied between $At = 0$ and $At = 0.5$, increasing the asymmetric concentration of baroclinically produced vorticity in thin and folded layers. The saturation of the primary KH mode is fixed at $t_{KH} = 30$ for all the cases considered. A direct-adjoint non-modal linear analysis is then used to determine the three-dimensional optimal perturbation growing over a single period of the VDKH billow. The temporal frame of optimisation is modified by varying both the injection time t_0 of the perturbation and the horizon time T at which the energy gain of the perturbation is required to be maximal.

When perturbations are injected at the initial time of the flow evolution, i.e. $t_0 = 0$, it is found that the Atwood number has no significant influence on their growth before a bifurcation time $t_b \approx 20$. For horizon times smaller than the bifurcation time, the optimal perturbations follow the same path for energy growth whatever the value of the Atwood number. During this period, the optimal energy growth is due to a combination of the classical Orr and lift-up mechanisms as already noticed by Arratia *et al.* (2013) in the homogeneous case. Perturbations with small spanwise wavenumber take more advantage from the Orr mechanism while perturbations with large wavenumber grow essentially thanks to the lift-up mechanism. When the horizon time is larger than the bifurcation time, the presence of mass inhomogeneities in the flow induces strong modifications on the base flow and optimal energy growth beyond t_b. First the energy gain is much larger than the one measured in the homogeneous case. As the horizon time is increased up to $T = 60$, the extra energy gain becomes more important for large wavenumber perturbation than for small wavenumbers ones. Nevertheless, the global optimal always correspond to a small wavenumber perturbation. Second, the route for energy growth totally differs from the one observed in the homogeneous mixing layer. The growth mechanism in the homogeneous case lies in the development of longitudinal counter-rotating vortices

https://doi.org/10.1017/jfm.2016.509 Published online by Cambridge University Press

located along the braid that eventually triggers the elliptic core-centred translative instability at small wavenumber and the hyperbolic braid-centred instability for large wavenumber (Arratia *et al.* 2013). In the variable-density case, the energy growth is associated with the emergence of longitudinal velocity streaks of opposite sign located along the braid on either side of the saddle point. These streaks are resulting from the development of elongated spanwise vorticity layers in the braid due to baroclinic vorticity production. Whatever the value of the spanwise wavenumber, the optimal perturbation is essentially located in the braid region which is the characteristic of a hyperbolic-type instability. The small wavenumber elliptic instability is not observed anymore. This new transitional scenario attests that the route to three-dimensionalisation of variable-density shear flows is very specific and cannot be simply transposed from the one observed in their homogeneous counterparts. It stands as an alternative to the generation mechanism of side jets proposed by Monkewitz & Pfizenmaier (1991) relying on the longitudinal rib vortices which are not present in the inhomogeneous case. Instead, it is more likely that side ejections in round jets would result from the convergence of the longitudinal velocity streaks near the braid saddle point. The relevance of such mechanism for side ejection should be assessed by numerical simulations of the nonlinear development of the optimal perturbations in order to examine the evolution of the velocity field in crosswise planes near the saddle point. It would be also interesting to see if the route to three-dimensionalisation observed here is recovered by performing a similar non-modal analysis in the case of variable-density round jets.

When the injection time is delayed so as to shorten significantly or even suppress the initial period of growth before the bifurcation time, a new family of perturbations is emerging at low wavenumbers. This branch exhibits a maximum of amplification in the two-dimensional limit, i.e. $k = 0$, and can reach energy gains far more larger than those measured so far when the injection time is increased up to t_b. These perturbations correspond to the two-dimensional secondary KH mode growing in the vorticity-enhanced braid of the primary structure originally discovered numerically by Reinaud *et al.* (2000) and retrieved later by Fontane & Joly (2008) by means of a modal stability analysis. The emergence of this new branch prefigures another route to turbulence through a fractal two-dimensional cascade already observed by Fontane *et al.* (2008). However, this two-dimensional KH secondary instability appears only for delayed perturbations which is unlikely to occur in natural mixing layers. This is probably why the secondary KH instability has never been observed in experimental set-up so far.

In the context of jet injectors found in combustion chambers, the aim is to improve the mixing between the fuel and the oxidiser. The recent work on channel flow due to Foures, Caulfield & Schmid (2014) showed that maximising the energy growth of the perturbation does not necessarily lead to an optimal mixing between passive scalars while minimising either the scalar variance or the so-called mix-norm introduced by Mathew, Mezic & Petzold (2005), proved to be much more efficient. We think there is some interest in testing these objective functions and to understand how the optimal perturbations differ from the present ones.

Appendix A. Linear matrix operators

The three linear matrix operators of the direct system (2.9) take the following form

https://doi.org/10.1017/jfm.2016.509 Published online by Cambridge University Press

(1) $\boldsymbol{N}_t$ the temporal operator:

$$\boldsymbol{N}_t = \begin{pmatrix} \dfrac{\partial \star}{\partial t} & 0 & 0 \\ 0 & \dfrac{\partial \star}{\partial t} & 0 \\ 0 & 0 & 0 \end{pmatrix}. \tag{A 1}$$

(2) $\boldsymbol{N}_c$ the operator of coupling between the base flow and the perturbation:

$$\boldsymbol{N}_c = \begin{pmatrix} \boldsymbol{U}\cdot\nabla\star + \nabla\boldsymbol{U}\cdot\star & -\dfrac{\star}{R^2}\nabla P & \dfrac{1}{R}\nabla\star \\ \nabla R\cdot\star + R\nabla\cdot\star & \boldsymbol{U}\cdot\nabla\star + D\star & 0 \\ \nabla\cdot\star & 0 & 0 \end{pmatrix}. \tag{A 2}$$

(3) $\boldsymbol{N}_d$ the diffusion operator:

$$\boldsymbol{N}_d = \begin{pmatrix} -\dfrac{1}{R}\left(\boldsymbol{\Delta}\star + \dfrac{1}{3}\nabla(\nabla\cdot\star)\right) & \dfrac{\star}{R^2}\left(\boldsymbol{\Delta}\boldsymbol{U} + \dfrac{1}{3}\nabla D\right) & 0 \\ 0 & 0 & 0 \\ 0 & \dfrac{1}{Sc}\boldsymbol{\Delta}\left(\dfrac{\star}{R}\right) & 0 \end{pmatrix}, \tag{A 3}$$

where $\star$ stands for the components of vector $\boldsymbol{q}$. The two linear matrix operators of the adjoint system (2.14) take the following form

(1) $\boldsymbol{N}_c^\dagger$ the adjoint operator of coupling between the base flow and the adjoint perturbation:

$$\boldsymbol{N}_c^\dagger = \begin{pmatrix} -\boldsymbol{U}\cdot\nabla\star - \star\nabla\cdot\boldsymbol{U} + \nabla\boldsymbol{U}^{\mathrm{T}}\cdot\star & -R\nabla\star & -\nabla\star \\ -\dfrac{1}{R^2}\nabla P\cdot\star & -\boldsymbol{U}\cdot\nabla\star & 0 \\ 0 & 0 & \nabla\cdot\left(\dfrac{\star}{R}\right) \end{pmatrix}. \tag{A 4}$$

(2) $\boldsymbol{N}_d^\dagger$ the adjoint diffusion operator:

$$\boldsymbol{N}_d^\dagger = \begin{pmatrix} -\boldsymbol{\Delta}\left(\dfrac{\star}{R}\right) - \dfrac{1}{3}\nabla\nabla\cdot\left(\dfrac{\star}{R}\right) & 0 & 0 \\ \dfrac{1}{R^2}\left(\boldsymbol{\Delta}\boldsymbol{U} + \dfrac{1}{3}\nabla D\right)\cdot\star & 0 & \dfrac{1}{ScR}\boldsymbol{\Delta}\star \\ 0 & 0 & 0 \end{pmatrix}. \tag{A 5}$$

Appendix B. The iterative optimisation algorithm

The iterative optimisation algorithm used to determine the optimal perturbation works as follow:

https://doi.org/10.1017/jfm.2016.509 Published online by Cambridge University Press

(1) Some perturbation $\boldsymbol{q}^{(\mathrm{i})}(t_0)$ is chosen as the initial condition for the direct system (2.9). Its kinetic energy and density amplitude are given by

$$\|\boldsymbol{q}(t_0)\|_u = E_0 \quad \text{and} \quad \|\boldsymbol{q}(t_0)\|_\rho = K_0, \tag{B 1}$$

where the semi-norms

$$\|\boldsymbol{q}\|_u = \|\boldsymbol{u}\| = [\boldsymbol{q} \mid \boldsymbol{W}^u \cdot \boldsymbol{q}] \tag{B 2}$$

and

$$\|\boldsymbol{q}\|_\rho = \|\rho\| = [\boldsymbol{q} \mid \boldsymbol{W}^\rho \cdot \boldsymbol{q}] \tag{B 3}$$

are associated with the inner product $[\star \mid \star]$ defined by

$$[\boldsymbol{q}_1 \mid \boldsymbol{q}_2] = \iint \boldsymbol{q}_1^* \cdot \boldsymbol{q}_2 \, \mathrm{d}x \, \mathrm{d}y + \text{c.c.}, \tag{B 4}$$

where the integration is performed on the numerical domain $[0, L_x] \times [-L_x/2, L_x/2]$, the exponent * stands for the complex conjugate and the matrix operators $\boldsymbol{W}^u$ and $\boldsymbol{W}^\rho$ are defined by

$$\boldsymbol{W} = \boldsymbol{W}^u + \boldsymbol{W}^\rho = \begin{pmatrix} 1 & 0 & 0 \\ 0 & 0 & 0 \\ 0 & 0 & 0 \end{pmatrix} + \begin{pmatrix} 0 & 0 & 0 \\ 0 & 1 & 0 \\ 0 & 0 & 0 \end{pmatrix}. \tag{B 5}$$

If any values for the constants E_0 and K_0 are possible in practice, they were fixed here to $E_0 = 1$ and $K_0 = 0$ for all cases. We did try non-zero values for K_0 but the results did not vary significantly from the case with no initial density perturbation. Furthermore, such configuration prefigures of an experimental control system where actuators only deviate the velocity field.

(2) The direct system (2.9) is advanced in time from the injection time t_0 up to the horizon time T with the linearised version of the pseudo-spectral method used for simulating the primary KH roll-up. As stated in Joly *et al.* (2005) and Joly & Reinaud (2007), we introduce modified density and pressure fields in order to compute the velocity in two steps as the combination of a solenoidal advection field and the pure dilatation resulting from mass diffusion. For the base flow they are defined as

$$\breve{\varrho} = \ln(R), \tag{B 6a}$$

$$\breve{\phi} = \frac{1}{R}\left(P - \frac{1}{3Re}\nabla \cdot \boldsymbol{U}\right), \tag{B 6b}$$

while for the perturbations they write

$$\varrho = \frac{\rho}{R}, \tag{B 7a}$$

$$\phi = \frac{1}{R}\left(p - \frac{1}{3Re}\nabla \cdot \boldsymbol{u}\right) - \varrho\breve{\phi}. \tag{B 7b}$$

Using these variables, the direct equations (2.8) transform into

$$\frac{\partial \boldsymbol{u}}{\partial t} = \boldsymbol{F}_u - \nabla\phi, \tag{B 8a}$$

https://doi.org/10.1017/jfm.2016.509 Published online by Cambridge University Press

$$\frac{\partial \varrho}{\partial t} = \boldsymbol{F}_{\varrho} + \frac{1}{Re\,Sc}\boldsymbol{\Delta}\varrho, \tag{B 8b}$$

$$\boldsymbol{\nabla}\cdot\boldsymbol{u} = -\frac{1}{Re\,Sc}\boldsymbol{\Delta}\varrho, \tag{B 8c}$$

where operators $\boldsymbol{F}_u$ and $\boldsymbol{F}_{\varrho}$ embody the coupling terms between the base flow and the perturbations:

$$\boldsymbol{F}_u = -\boldsymbol{U}\cdot\boldsymbol{\nabla}\boldsymbol{u} - \boldsymbol{u}\cdot\boldsymbol{\nabla}\boldsymbol{U} - \phi\boldsymbol{\nabla}\breve{\varrho} - \breve{\phi}\boldsymbol{\nabla}\varrho + \frac{1}{Re\,R}(\boldsymbol{\Delta}\boldsymbol{u} - \varrho\boldsymbol{\Delta}\boldsymbol{U}), \tag{B 9a}$$

$$\boldsymbol{F}_{\varrho} = -\boldsymbol{U}\cdot\boldsymbol{\nabla}\varrho - \boldsymbol{u}\cdot\boldsymbol{\nabla}\breve{\varrho}. \tag{B 9b}$$

(3) The energy gain $G_E^{(\mathrm{i})}$ of the perturbation is computed as defined by (2.11). If the criterion $(G_E^{(\mathrm{i})} - G_E^{(\mathrm{i}-1)})/G_E^{(\mathrm{i}-1)}$ is below a chosen threshold, the method has converged towards the optimal perturbation. Otherwise, we turn to the next step.

(4) The final state of the perturbation $\boldsymbol{q}(T)$ is used to compute the initial condition for the adjoint system (2.14):

$$\boldsymbol{W}\cdot\boldsymbol{q}^{\dagger}(T) = \boldsymbol{W}^{u}\cdot\boldsymbol{q}(T). \tag{B 10}$$

(5) The adjoint system (2.14) is advanced backward in time from T to t_0 with the same numerical pseudo-spectral method used for the direct equations. Similarly, we define modified velocity and pressure adjoint variables for the perturbation

$$\boldsymbol{v}^{\dagger} = \frac{\boldsymbol{u}^{\dagger}}{R}, \tag{B 11a}$$

$$\phi^{\dagger} = \frac{p^{\dagger}}{R}. \tag{B 11b}$$

With these modified fields, the adjoint equations (2.13) transform into

$$-\frac{\partial \boldsymbol{v}^{\dagger}}{\partial t} = \boldsymbol{F}_{\upsilon}^{\dagger} + \boldsymbol{\nabla}\phi^{\dagger} + \boldsymbol{\nabla}\rho^{\dagger}, \tag{B 12a}$$

$$-\frac{\partial \rho^{\dagger}}{\partial t} = \boldsymbol{F}_{\rho}^{\dagger}, \tag{B 12b}$$

$$\boldsymbol{\nabla}\cdot\boldsymbol{v}^{\dagger} = 0, \tag{B 12c}$$

where operators $\boldsymbol{F}_{\upsilon}^{\dagger}$ and $\boldsymbol{F}_{\rho}^{\dagger}$ include the coupling terms between the base flow and the adjoint perturbations:

$$\boldsymbol{F}_{\upsilon}^{\dagger} = \boldsymbol{U}\cdot\boldsymbol{\nabla}\boldsymbol{v}^{\dagger} - \boldsymbol{v}^{\dagger}\cdot\boldsymbol{\nabla}\boldsymbol{U}^{\mathrm{T}} + \phi^{\dagger}\boldsymbol{\nabla}\breve{\varrho} + \frac{1}{ReR}\boldsymbol{\Delta}\boldsymbol{v}^{\dagger}, \tag{B 13a}$$

$$\boldsymbol{F}_{\rho}^{\dagger} = \boldsymbol{U}\cdot\boldsymbol{\nabla}\rho^{\dagger} + \boldsymbol{v}^{\dagger}\cdot\left(\boldsymbol{\nabla}\breve{\phi} + \breve{\phi}\boldsymbol{\nabla}\breve{\varrho} - \frac{1}{ReR}\boldsymbol{\Delta}\boldsymbol{U}\right) - \frac{1}{Re\,Sc\,R}\boldsymbol{\Delta}p^{\dagger}. \tag{B 13b}$$

(6) At the injection time t_0, the new initial condition $\boldsymbol{q}^{(\mathrm{i}+1)}(t_0)$ is obtained through the optimality condition

$$\Lambda_u\boldsymbol{W}^{u}\cdot\boldsymbol{q}(t_0) + \Lambda_{\rho}\boldsymbol{W}^{\rho}\cdot\boldsymbol{q}(t_0) - \boldsymbol{q}^{\dagger}(t_0) = 0, \tag{B 14}$$

where Lagrange multipliers Λ_u and Λ_{ρ} are chosen so as to rescale the velocity and density fields with respect to (B 1). Then we go back to step 2 until the convergence is reached.

https://doi.org/10.1017/jfm.2016.509 Published online by Cambridge University Press

REFERENCES

ARRATIA, C., CAULFIELD, C. P. & CHOMAZ, J.-M. 2013 Transient perturbation growth in time-dependent mixing layers. *J. Fluid Mech.* **717**, 90–133.

BATCHELOR, G. 1967 *An Introduction to Fluid Mechanics*. Cambridge University Press.

BRANCHER, P., CHOMAZ, J.-M. & HUERRE, P. 1994 Direct numerical simulations of round jets: vortex induction and side jets. *Phys. Fluids* **6** (5), 1768–1774.

CAULFIELD, C. P. & KERSWELL, R. R. 2000 The nonlinear development of three-dimensional disturbances at hyperbolic stagnation points: a model of the braid region in mixing layers. *Phys. Fluids* **12** (5), 1032–1043.

CAULFIELD, C. P. & PELTIER, W. R. 2000 The anatomy of the mixing transition in homogeneous and stratified free shear layers. *J. Fluid Mech.* **413**, 1–47.

CORBETT, P. & BOTTARO, A. 2000 Optimal perturbations for boundary layers subject to stream-wise pressure gradient. *Phys. Fluids* **12**, 120–130.

CORBETT, P. & BOTTARO, A. 2001 Optimal linear growth in swept bounday layers. *J. Fluid Mech.* **435**, 1–23.

CORCOS, G. M. & LIN, S. J. 1984 The mixing layer: deterministic models of a turbulent flow. Part 2. the origin of three-dimensional motion. *J. Fluid Mech.* **139**, 67–95.

CORTESI, A. B., YADIGAROGLU, G. & BANERJEE, S. 1998 Numerical investigation of the formation of three-dimensional structures in stably-stratified mixing layers. *Phys. Fluids* **10** (6), 1449–1473.

DAVEY, R. F. & ROSHKOM, A. 1972 The effect of a density difference on shear-layer instability. *J. Fluid Mech.* **53**, 523–543.

DIXIT, H. N. & GOVINDARAJAN, R. 2010 Vortex-induced instabilities and accelerated collapse due to inertial effects of density stratification. *J. Fluid Mech.* **646**, 415–439.

DRITSCHEL, D. G., HAYNES, P. H., JUCKES, M. N. & SHEPPERD, T. G. 1991 The stability of a two-dimensional vorticity filament under uniform strain. *J. Fluid Mech.* **230**, 647–665.

ELLINGSEN, T. & PALM, E. 1975 Stability of linear flow. *Phys. Fluids* **18** (4), 487–488.

FARRELL, B. 1988 Optimal excitation of perturbations in vicous shear flow. *Phys. Fluids* **5** (11), 2600–2609.

FARRELL, B. F. & IOANNOU, P. J. 1993 Optimal excitation of three-dimensional perturbations in viscous constant shear flow. *Phys. Fluids* A **612** (6), 1390–1400.

FONTANE, J. 2005 Transition des écoulements cisaillés libres à densité variable. PhD thesis, Institut National Polytechnique de Toulouse.

FONTANE, J. & JOLY, L. 2008 The stability of the variable-density Kelvin–Helmholtz billow. *J. Fluid Mech.* **5**, 237–260.

FONTANE, J., JOLY, L. & REINAUD, J. N. 2008 Fractal Kelvin–Helmholtz break-ups. *Phys. Fluids* **20** (9), 091109.

FOURES, D. P. G., CAULFIELD, C. P. & SCHMID, P. J. 2014 Optimal mixing in two-dimensional plane poiseuille flow at infinite Péclet number. *J. Fluid Mech.* **748**, 241–277.

GUNZBURGER, M. 2003 *Perspectives in Flow Control and Optimization*. SIAM.

JOLY, L. 2002 The structure of some variable density shear flows. In *Variable Density Fluid Turbulence* (ed. P. Chassaing, R. A. Antonia, F. Anselmet, L. Joly & S. Sarkar), chap. 8, pp. 201–234. Springer.

JOLY, L., FONTANE, J. & CHASSAING, P. 2005 The Rayleigh–Taylor instability of two-dimensional high-density vortices. *J. Fluid Mech.* **537**, 415–431.

JOLY, L. & REINAUD, J. N. 2007 The merger of two-dimensional radially stratified high-Froude-number vortices. *J. Fluid Mech.* **582**, 133–151.

JOLY, L., REINAUD, J. N. & CHASSAING, P. 2001 The baroclinic forcing of the shear layer three-dimensional instability. In *2nd International Symposium on Turbulence and Shear Flow Phenomena, Stockholm*, vol. 3, pp. 59–64.

JOLY, L., SUAREZ, J. & CHASSAING, P. 2003 The strain field of light jets. In *5th European Fluid Mechanics Conference*.

https://doi.org/10.1017/jfm.2016.509 Published online by Cambridge University Press

JOSEPH, D. D. 1990 Fluid dynamics of two miscible liquids with diffusion and gradient stresses. *Eur. J. Mech. (B/Fluids)* **9**, 565–596.

KAMINSKI, A. K., CAULFIELD, C. P. & TAYLOR, J. R. 2014 Transient growth in strongly stratified shear layers. *J. Fluid Mech.* **758**, R4.

KLAASSEN, G. P. & PELTIER, W. R. 1985 The onset of turbulence in finite-amplitude Kelvin–Helmholtz billows. *J. Fluid Mech.* **155**, 1–35.

KLAASSEN, G. P. & PELTIER, W. R. 1991 The influence of stratification on secondary instability in free shear layers. *J. Fluid Mech.* **227**, 71–106.

KNIO, O. M. & GHONIEM, A. F. 1992 The three-dimensional structure of periodic vorticity layers under non-symmetric conditions. *J. Fluid Mech.* **243**, 353–392.

LANDHAL, M. T. 1975 Wave breakdown and turbulence. *SIAM J. Appl. Maths* **28** (4), 735–756.

LANDHAL, M. T. 1980 A note on an algebraic instability of inviscid parallel shear flows. *J. Fluid Mech.* **98** (2), 243–251.

LASHERAS, J. C. & CHOI, H. 1988 Three-dimensional instability of a plane free shear layer: an experimental study of the formation and evolution of streamwise vortices. *J. Fluid Mech.* **189**, 53–86.

LOPEZ-ZAZUETA, A. 2015. Stabilité secondaire non-modale d'une couche de mélange inhomogène. PhD thesis, Université de Toulouse, Institut Supérieur de l'Aéronautique et de l'Espace.

LUCHINI, P. & BOTTARO, A. 1998 Görtler vortices: a backward-in-time approach to the receptivity problem. *J. Fluid Mech.* **363**, 1–23.

MATHEW, G., MEZIC, I. & PETZOLD, L. 2005 A multiscale measure for mixing. *Physica* D **211**, 23–46.

METCALFE, R. W., ORSZAG, S. A., BRACHET, M. E., MENON, S. & RILEY, J. J. 1987 Secondary instability of a temporally growing mixing layer. *J. Fluid Mech.* **184**, 207–243.

MONKEWITZ, P. A., BECHERT, D. W., BARSIKOW, B. & LEHMAN, B. 1990 Self-excited oscillations and mixing in a heated round jet. *J. Fluid Mech.* **213**, 611–639.

MONKEWITZ, P. A., LEHMANN, B., BARSIKOW, B. & BECHERT, D. W. 1989 The spreading of self-excited hot jets by side jets. *Phys. Fluids* A **1** (3), 446–448.

MONKEWITZ, P. A. & PFIZENMAIER, E. 1991 Mixing by 'side-jets' in strongly forced and self-excited round jets. *Phys. Fluids* A **3** (5), 1356–1361.

ORR, W. M. 1907*a* The stability or instability of the steady motions of a perfect liquid and of a viscous liquid. Part 1: a perfect liquid. *Proc. R. Irish Acad.* **27**, 9–68.

ORR, W. M. 1907*b* The stability or instability of the steady motions of a perfect liquid and of a viscous liquid. part 2: a viscous liquid. *Proc. R. Irish Acad.* **27**, 69–138.

PIERREHUMBERT, R. T. & WIDNALL, S. E. 1982 The two- and three-dimensional instabilities of a spatially periodic shear layer. *J. Fluid Mech.* **144**, 59–82.

REINAUD, J., JOLY, L. & CHASSAING, P. 2000 The baroclinic secondary instability of the two-dimensional shear layer. *Phys. Fluids* **12** (10), 2489–2505.

ROGERS, M. & MOSER, R. 1992 The three-dimensional evolution of a plane mixing layer: the Kelvin–Helmholtz rollup. *J. Fluid Mech.* **243**, 183–226.

SANDOVAL, D. L. 1995 The dynamics of variable-density turbulence. PhD thesis, University of Washington.

SCHMID, P. J. 2007 Nonmodal stability theory. *Annu. Rev. Fluid Mech.* **39**, 129–162.

SCHOWALTER, D., VAN ATTA, C. & LASHERAS, J. 1994 A study of streamwise vortex structure in a stratified shear layer. *J. Fluids Mech.* **281**, 247–292.

SOTERIOU, M. C. & GHONIEM, A. F. 1995 Effect of the free-stream density ratio on free and forced spatially developing shear layers. *Phys. Fluids* A **7** (8), 2036–2051.

https://doi.org/10.1017/jfm.2016.509 Published online by Cambridge University Press